INVESTIGATING PROTON TRANSFER DYNAMICS AT THE TUNGSTEN OXIDE THIN-FILM INTERFACE

by

NADIA F. BARNARD

A THESIS

Presented to the Department of Chemistry
and the Robert D. Clark Honors College
in partial fulfillment of the requirements for the degree of
Bachelor of Science

MAY 2025

An Abstract of the Thesis of

Nadia F. Barnard for the degree of Bachelor of Science
in the Department of Chemistry to be taken June 2025

Title: Investigating Proton Transfer Dynamics at the Tungsten Oxide Thin-Film Interface

Approved: *Paul Kempler, Ph.D.*
Primary Thesis Advisor

Investigating the kinetics of interfacial ion transfer is critical for understanding improvements to electrochemical energy storage systems, such as cation batteries. While there is an established electron transfer theory, pioneered by Marcus, ion transfer at electrochemical interfaces is poorly understood. Even extensively studied systems, such as $LiFePO_4$, exhibit resistive behavior and convoluted ion transfer mechanisms. To avoid this limitation, metal oxides can provide a simpler model for studying kinetics and offer benefits relevant to materials development for electrochemical devices with their enhanced charge capacity and tunability. Consequently, we study proton transfer mechanisms at metal-oxide/liquid interfaces to evaluate key parameters that could optimize battery efficiency and electrocatalysis. Using electrochemical techniques, we aim to deconvolute the mechanistic and rate-limiting factors associated with proton insertion from an acidic aqueous electrolyte into a thin film of tungsten trioxide (WO_3).

While WO_3 has been investigated as a negative electrode for batteries, the kinetics of cation insertion remain inadequately explored despite their effects on system efficiency. Using current transients, exchange current densities and rate constants for cation insertion were studied across a range of quasi-equilibrated states of charge.[1] A $KHSO_4$ buffer system of various

strengths was used to explore the identity of the proton donor for WO_3 insertion. Proton insertion kinetics are independent of buffer concentration for potassium bisulfate indicating that hydronium outcompetes bisulfate as the proton donor in solution. However, a phosphoric acid ($H_2PO_4^-/H_3PO_4$) buffer solution exhibited a minimal amount of proton-donor concentration dependence for the proton insertion reaction. This finding shows that proton insertion in transition metal oxides can be accelerated by extraneous solvent properties to lower applied overpotentials. Here, the broader implications for interfacial ion transfer phenomena can evolve our understanding of energy storage and conversion processes.

Acknowledgments

I would like to extend my deepest gratitude towards Dr. Paul Kempler and Dr. Shannon Boettcher for supporting my work and providing the space and resources to perform my laboratory experiments. I would like to thank Dr. Rebecca Altman for being on my thesis committee as the Clark Honors College representative. I would also like to thank my graduate mentor, Nicholas D'Antona for providing immense help with this project, guiding my scientific education, and inspiring me to continue in electrochemistry. I appreciate the Boettcher and Kempler research groups for fostering a learning environment that has supported me through my undergraduate degree and encouraged me to specialize in electrochemistry through the Accelerated Master's Program. Lastly, I could not have achieved this without the support of my best friend and study partner, Caitlyn Cannan. Without the continued support of everyone mentioned and more, I would not be here today pursuing my newfound lifelong passion of electrochemistry.

Table of Contents

List of Figures

Research Questions

1. Can we model proton insertion kinetics in metal oxides using Butler-Volmer analysis?
2. Are there phase transitions within the WO_3 crystal lattice upon proton insertion?
3. How do different electrolyte compositions change the kinetics of proton insertion into a tungsten oxide thin-film electrode?
4. What species donates its proton in the proton insertion mechanism? Under what conditions will we observe more exchange current density?
5. How does an improved understanding of ion transfer contribute to scientific renewable energy efforts?

Introduction

Deep decarbonization offers a critical solution to mitigate climate change by aiding the transition to net-zero carbon technologies across various sectors. Electrochemical advancements will continue to prompt electrification across the grid, holding immense potential for enabling the conversion to reliance on clean energy. Ion transfer mechanisms are prevalent in electrochemical systems such as batteries, fuel cells, and carbon capture technologies, yet are understudied and poorly understood. Ion transfer is a fundamental yet often rate-limiting kinetic factor for many essential renewable energy systems, which are projected to be key factors in decarbonizing our electrical grid. Understanding the mechanisms and kinetics of ion insertion is critical to advancing technologies that rely on coupled ionic and electronic transport processes. This research aims to elucidate the intrinsic kinetic behavior of proton transfer at a model metal oxide system, focusing on how ions participate in concerted electron transfer pathways at electrochemical interfaces.

This thesis specifically investigates the kinetics of proton transfer in tungsten oxide, a promising electrode material with potential applications for sustainable energy storage. Tungsten oxide's ability to reversibly insert protons make it a compelling candidate for use in high-capacity charge storage systems. More importantly, a better understanding of ion transfer is thought through an analysis of ion transfer within tungsten oxide, which has the potential to apply to a multitude of electrochemical systems beyond charge storage. Electrochemical phenomena were modeled for the proton insertion reaction in tungsten oxide using basic electrochemical kinetic theory. Consequently, Butler-Volmer analysis of current transient responses were used to quantify the intrinsic rate of proton insertion into tungsten oxide.

Furthermore, the influence of different buffer environments on reaction kinetics was probed to determine the dominant proton donor species under varying pH and ionic strength conditions.

A significant challenge in investigation of interfacial ion transfer reactions is the competing faradaic and non-faradaic current response from reduction-oxidation and capacitive phenomena. To address this, a model equation representing the current transient response was used to isolate the ion transfer current and double layer charging current. By deconvoluting the response of these processes, a clearer understanding of concerted ion transfer can be approached, offering insights that may inform future renewable energy systems.

Literature Review: The Role of Kinetics in Renewable Energy Systems

This section outlines the background motivation for the following study of kinetics of proton insertion, which is deeply rooted in the global effort to address climate change. Kinetic models used to explain the transfer of ions in renewable energy systems often rely on purely empirical relationships, which lack the support of fundamental chemical principles. In this case, an empirical relationship would be one that was made based on observation of a system rather than the underlying theory. Bridging this gap with a more mechanistic understanding will not only strengthen the theoretical foundation but also extend to applied sectors of electrochemical science. By deepening our understanding of interfacial ion transfer in renewable energy devices, we may develop these technologies more effectively with a renewed perspective.

Renewable Energy and Decarbonization

Worldwide industrial development in the 1850s marked the beginning of a profound and lasting impact on the environment. It is well known that human influence has shaped the global climate, leading to a rapid increase in temperature after industrial processes began to dominate global economies and communities.[2] The primary reason for this alarmingly rapid temperature increase is carbon dioxide and subsequent heat-trapping gases produced as a derivative of human activity. Figure 1 shows the observed increase in temperature to ~1.25 °C above pre-industrial temperatures compared to the projected temperature change with no human contributions between 1850 and 2020.

Figure 1: The Effect of Human Influence on Global Temperatures

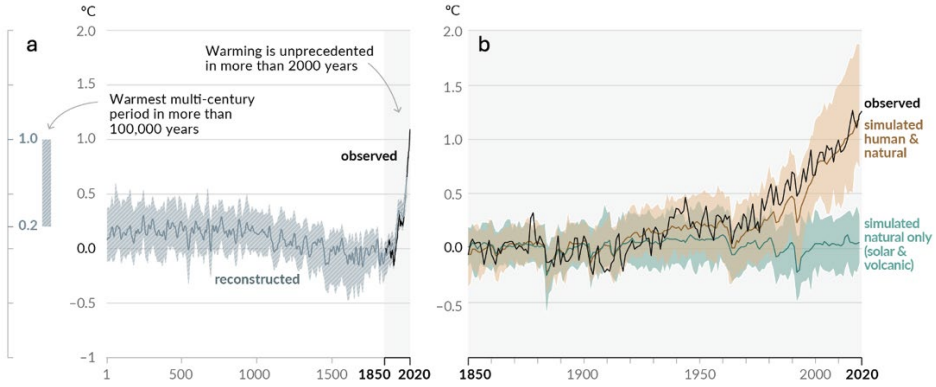

Figure 1: Two graphs convey the effect of human influence on the global surface temperature at a higher rate than predicted based on observations over the past 2000 years. In plots a) the decadal average of global surface temperature was reconstructed, where the section of years 1850 – 2020 is shown in b) where the combination of human and natural factors is shown to accelerate the global temperature increase. Figure sourced from the Intergovernmental Panel on Climate Change (IPCC).

Figure 2: Carbon Dioxide Emissions in the United States (1990 – 2023)

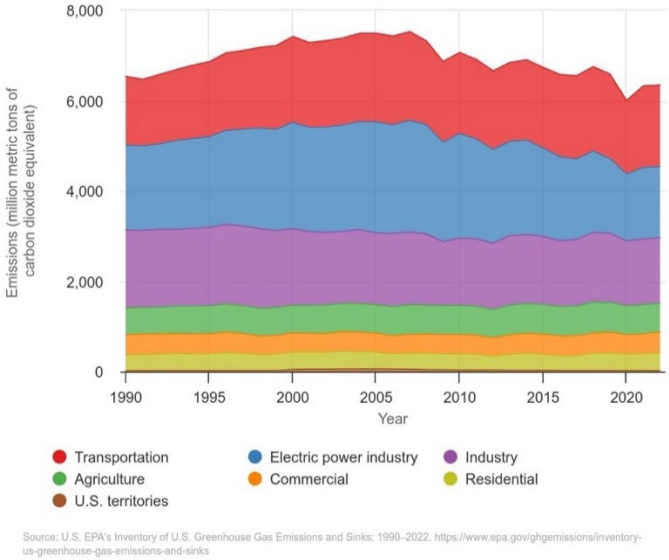

Figure 2: From the Environmental Protection Agency (EPA), the emissions of carbon dioxide are shown for each output sector, including transportation, electricity, and industrial sources, for every year since 1990.

Furthermore, Figure 2 shows the emissions of carbon dioxide in the United States over the years from 1990 to 2022, as monitored by the Environmental Protection Agency (EPA).[3] Here, the largest carbon dioxide contributors are transportation and electric power industry, closely followed by industrial sources. These emissions must be drastically decreased to decelerate the global temperature rise indicated in Figure 1. Notably, emissions from electric power have decreased over the years, likely due to integration of renewable energy sources. However, carbon dioxide emissions in the Unites States remains consistently above 5 billion metric tons per year.[3] A targeted effort to expand the renewable energy infrastructure is needed to reduce this emission to net-zero.

As the threat of climate crisis looms, deep decarbonization is a pathway to mitigate harmful carbon emissions and build a new economy and infrastructure reliant on renewable energy. Deep decarbonization is the notion that every sector should systematically reduce anthropogenic carbon emissions associated with industrial and consumer processes. The Paris Agreement has set an ambitious target for a 43% decrease in global carbon emissions by 2030 in an attempt to limit the global temperature increase to $< 2°C$.[4] In order to accomplish this, a rapid deployment of alternatives to carbon-emitting technologies will be needed, including sectors of transportation, agriculture, construction, and energy.[5] To keep up with the technological demands of limiting greenhouse gas (GHG) output, countries will rely on scientific advancements in conjunction with political cooperation. With a larger emphasis on research and development, financial support written into policy, and infrastructure enhancement, these aspirations can be attained.

Our energy systems must be designed to account for fluctuations in energy supply to accommodate for the growing energy demand with renewable energy infrastructure

development. As temperatures increase, the global energy usage will continue to grow and compound carbon emissions if renewable energy production is not implemented.[6] Clean energy storage systems which can be deployed on large scales are needed to accelerate the transition to reliance on renewable energy. For example, solar energy has limited daytime production and produces power at different peak times depending on the time of day and season. A reliable and durable energy storage system with minimal losses would expand the feasible applications for clean energy sources. Other manners of harboring energy for future use, like storing excess electrical energy within stable chemical bonds, may also contribute to the transition.

Advanced scientific techniques must be developed to electrify carbon-emitting technologies that mitigate climate change. A key area of science, electrochemistry, will be crucial for making deep decarbonization a reality.[7] Electrochemistry enables the use of electrical energy to push forward a non-spontaneous chemical reaction or the extraction of electrical energy from a spontaneous chemical reaction. All energy storage technologies, like batteries and hydrogen conversion, involve electrons and ions transferring through the system in some capacity. In the case of batteries, ions reversibly move between electrodes upon charging and discharging. For water electrolysis or hydrogen fuel cell systems, ions repeatedly move across diaphragms or membranes to separate from their reactant counterparts to be evolved into the product. For such a crucial reaction component, ion transfer is often a convoluted occurrence which varies throughout systems, leaving the concept ill-defined. Investigating ion transfer within complex electrochemical systems will encourage a renewed perspective for developing systems that operate with heightened consideration for such mechanisms.

To address this task, we employ the unique techniques of electrochemistry to develop potential energy-saving and carbon-reducing technologies. The progression of electrochemical

systems with the purpose of charge storage, carbon capture, water electrolysis, and even water treatment presents the forefront of electrification.[7,8] The use of electricity to manipulate and prompt chemical reactions is an advancing and versatile field that leads the way in both academia and policy.

Tungsten Oxide

Figure 3: Tungsten Oxide Crystal Lattice Model

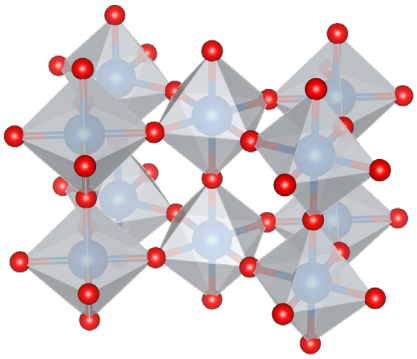

Figure 3: Tungsten oxide crystal lattice in a monoclinic structure. Here, the blue atoms are tungsten (W), and red atoms are oxygen (O). Photo created with VESTA.

This thesis explores the electrochemical behavior of proton insertion in tungsten trioxide (WO_3), as seen in Figure 3. WO_3 is typically used in electrochromic applications, where it reversibly changes color as electricity is applied.[9] Electrochromic films are used in smart windows to conserve heating and cooling energy expenses, due to their electrochemical stability and reversibility.[10] Another emerging application for WO_3 is as a negative battery electrode. Batteries rely on the continual cycle of insertion and de-insertion of charge to generate power, so it is important to apply these concepts to how tungsten oxide responds mechanistically in insertion conditions.

WO_3 is easy to functionalize, or change structure, and has high stability at low pHs.[11,12] These characteristics allow for a wide range of chemical modifications, like doping or creating

nanostructures, which can tailor the electrochemical behaviors. As a result, WO_3 has satisfactory charge transport and corrosion resistance properties, making it ideal for a battery electrode material for charge storage or a supercapacitor.[13]

Recent efforts to understand ion transfer studies are done with annealed Au (111) electrodes to minimize discrepancies in surface energies across the electrode.[14] However, electrochemical charge storage materials are often composed of porous electrode materials, like transition metal oxides, which have more relevance in the field. In practical battery applications where porous electrodes insert ions to store charge, organic solvents are used, causing the formation of a passivation solid-electrolyte interface (SEI) layer, further complicating ion transfer mechanisms. To mitigate these convolutions, an aqueous electrolyte solution is used in a small pH range to minimize possible side reactions that could otherwise deter rate calculations. In an acidic aqueous electrolyte, proton insertion into a tungsten oxide thin film is evaluated for its kinetics.

Most studies involving WO_3 solely consider the hydrogen evolution reaction (HER) and how it's reaction kinetics are improved upon hydrogenation or hydration of tungsten oxide lattice. Miu et al. reported that kinetics for the HER were dependent on the degree of protonation as well, with higher HER activity observed for protonated tungsten oxides, providing insight into the physical transitions experienced by tungsten oxide during the insertion process.[15] Furthermore, Mitchell et al. reported the improved capacity and kinetic activity of hydrated tungsten oxides and classified the mode of diffusion through $WO_3 \cdot H_2O$ films as a Grothuss proton hopping mechanism.[16,17] Grothuss proton hopping proceeds as protons transfer through the hydrated transition metal oxide by 'hopping' from each metal or oxygen center. Once this occurs at one center, it sets off a chain reaction, encouraging nearby protons to continue

movement through a lattice, resulting in a rapid proton transport network. However, Lin et al. concluded that for non-hydrated WO_3, protons diffuse through the film without the influence of structural water and instead proceeds by moving about the corners of the WO_3 octahedron.[18]

While these studies highlighted the hydrogen evolution reaction at cathodic overpotentials in WO_3, the proton insertion mechanism for proton insertion and the role of solvent environment has received less attention. Equation 1 shows the hydrogenation of WO_3 to form a tungsten bronze and water after proton transfer. The stoichiometry coefficient, x, is the measure of the degree of protonation, which depends on the magnitude of the applied overpotential and the electrolyte composition.

$$WO_3 + xH_3O^+ + e^- \rightarrow H_xWO_3 + \mathrm{xH_2O}\ [1]$$

Electrochemical Kinetics

Electrochemical reactions are primarily dictated by thermodynamics, kinetics, and mass transport. Electrochemical reactions can be limited by the transport of materials to the electrode surface, charge transfer of electrons through the electrode material, ion transfer of species from solution, or more.[19] Since electrons are much smaller and less massive than ions, their transfer is often easier, such that ion transfer is the rate-limiting factor in many electrochemical systems. Often, the resistance towards ion movement through a solution or transfer at the surface of or into an electrode is a dominating concern. Ion movement is not well understood within the field, even though it often contributes significantly the systemic efficiency of many larger-scale renewable energy processes. By studying this process, we hope to address the apparent knowledge gap and design model systems that consider kinetics more appropriately.

The movement of electrons and ions in an electrochemical system is governed by both electric and chemical forces, each contributing to the overall energy cost of the reaction. Electrons are supplied to the system by a current collector, often a Potentiostat or electrode, when a reducing (negative) voltage is applied, then diffuse through the solid electrode to the surface. To balance this reaction, cations in the outer solution migrate towards the negative charge. Migration is the movement of species in response to an applied electrical field. However, during this movement through the electrolyte, ions are 'solvated' or supported by surrounding water molecules. This phenomenon occurs in response to formal charge balancing, and a cation in aqueous solution will have formally negative oxygen molecules from H_2O surrounding it. To complete a transfer of ions, the solvated ion must shed its outer layer(s) of supporting water molecules. This is an energy-intensive process likely to consume a large portion of the applied overpotential, contributing to rate considerations.[20] Overpotential is the deviation of applied or measured potential from the equilibrium potential.

An important inhibitive element in ion transfer from solution is diffusion, or movement caused by a concentration gradient.[20] When species are consumed on the surface of an electrode, a concentration gradient is created. Diffusion explains how molecules move through a solution to make up for this sharp concentration change over space. Fick's first law of diffusion (Equation 1) relates the reaction flux (J) to the concentration gradient ($\frac{\partial C}{\partial x}$) and diffusion coefficient (D), where a steeper gradient results in a higher flux. A diffusion-limited current can be reached when the rate of diffusion is at its fastest and the maximum number of species is transferred to the surface. In battery materials and transition metal oxides, diffusion can occur both through the electrolyte solution and within the porous electrode material itself, introducing additional considerations like tortuosity, pore connectivity, and phase transformations within the active material.[16] Much effort

has been directed to evaluating the limitations of lithium-ion batteries, and how ion transfer plays a role in battery cells. However, newer materials, like tungsten oxide, have not received as much attention regarding their interfacial ion transfer properties.

$$J = -D\frac{\partial C}{\partial x} \text{ [2]}$$

The kinetics of an electrochemical reaction are often modeled with the Butler -Volmer equation, in Equation 1. Here, j is the current density extracted from a measurement, j_0 is the exchange current density, α terms are the charge transfer coefficients, η is the overpotential from an established equilibrium, F is Faraday's constant, z is the charge of species, R is the ideal gas constant, and T is the temperature of the system. The charge transfer coefficient refers to the symmetry of the reaction and ranges from 0 – 1 to indicate which direction the reaction is favored towards. While the Butler-Volmer equation is a useful diagnostic assessment of reaction kinetic, it fails to provide chemical intuition for the mechanism of charge transfer, leading to the use of Marcus theory.

$$j = j_0\left(e^{\left(\frac{\alpha_a zF\eta}{RT}\right)} - e^{\left(\frac{\alpha_c zF\eta}{RT}\right)}\right) \text{ [3]}$$

Electron and Ion Transfer

Figure 4: Illustration of the Electrochemical Double Layer

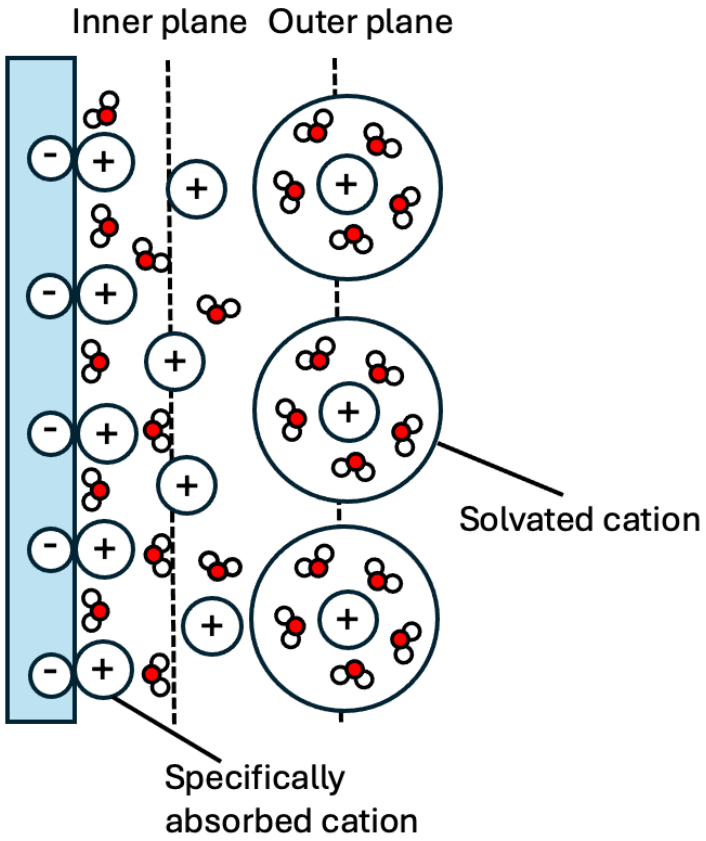

Figure 4: Double layer charging schematic at an electrode/electrolyte interface. Ions orient at the surface differently depending on their proximity to the electrode, where the outer plane houses completely solvated cations and the inner plane has specifically adsorbed cations on the surface of the electrode.

The electrochemical double layer is the buildup of opposing charges on both side of an interface, as denoted in Figure 4, where a negative charge is applied to the electrode. Within the electrochemical double layer are several layers composed of ion and solvent molecules whose orientation is dependent on their proximity of the electrode. Within the outer plane, there are fully solvated ions which are surrounded by solvent molecules in solution to minimize the system's energy. Within the inner plane, ions are specifically absorbed to the surface while solvent molecules disband themselves from the ion.

The electrochemistry field has established a well-accepted proposal for the mechanics of electron transfer, dubbed Marcus theory, yet lacks an encompassing framework for ion transfer. Electron transfer reactions are classified as either inner-sphere or outer-sphere when considering a chemical change between an electroactive ion in solution and an electrode.[20] In an outer-sphere reaction, the solvated ion approaches the electrode surface and remains outside the outer plane of the double-layer during electron transfer, as seen in Figure 4. In contrast, an inner-sphere reaction entails chemical contact between an ion and the electrode surface, where the ion adsorbs to complete an electron transfer. The electron must travel different distances in these cases, either traversing through the electrochemical double layer or to the surface.

In reactions that require electrons to cross the double layer, Marcus theory proposes that electrons tunnel through the double layer in response to the electronic rearrangement of surrounding orbitals, prompting a spectroscopic, radiation-less electronic transition at the electrode.[21] This electron tunneling can only occur when the reactant overcomes an activation barrier to reach a configuration where is can successfully accept an electron. This activation energy was found to be directly related to the rate of the reaction, which causes the current to increase exponentially with applied overpotential at a scale dictated by the kinetic parameters of a system in an Arrhenius-like relationship. The core equation from Marcus theory is expressed in Equation 4, where the electron transfer rate constant, k_{ET} is expressed by the following relationship where A is a pre-exponential coefficient, λ is the solvent reorganization energy, ΔG^0 is the change in standard Gibbs free energy, k_B is the Boltzmann constant, and T is temperature.

$$k_{ET} = Aexp\left[\frac{-(\lambda+\Delta G^0)^2}{4\lambda k_B T}\right] \qquad [4]$$

Equation 4 initially predicted that increasing the driving force of the reaction with a more negative ΔG^0 would always enhance the rate electron transfer, given by the exponential relationship. However, experimentation showed that reactions rates actually decreased at high applied driving forces. To account for this discrepancy between theory and observed experimentation, Marcus theory eventually evolved into Marcus-Hush-Chidsey (MHC).[21] Chidsey's contributions extended the original framework to describe interfacial electron transfer processes to account for the theoretical deviation from classical charge transport behavior into an "inverted region". While basic Marcus theory predicted that an increase in driving force would always cause an increase in reaction rate, MHC theory accounts for a paradoxical decrease in reaction rate at high driving force applications which occurs in the inverted region. This led to a deeper understanding of non-linear kinetic relationships in electron transfer theory and helped bridge the gap between electrochemical theory and experimentation.

Henstridge et al. applied MHC formalism to electrode reactions, where the comparison between MHC and Butler-Volmer kinetic models revealed how extra parameters like solvent reorganization energies and changes in the charge transfer coefficient based on overpotential were necessary to capture observed rates.[21] The heterogeneous rate constant indicates the facility of electron transfer and is influenced by the solvent reorganization dynamics in solution. This alludes to a complicated relationship between the electron and the receiving ion, where the ability of electron transfer is inherently impacted by the qualities of the electrolyte solution. Bai and Bazant used both MHC and BV theory to evaluate ion insertion into a porous electrode, $LiFePO_4$, which is a common battery cathode. The authors found that current transient measurements are difficult to model at porous electrode surfaces due to consequential phase transformations or non-uniform reaction rates.[22] Since previous studies have struggled to

accurately study ion transfer kinetics due to electrode phase transformations and time-dependent reaction rates, this study approaches the issues by using a model system.

Figure 5: Solvation and Desolvation of Anions in PCET

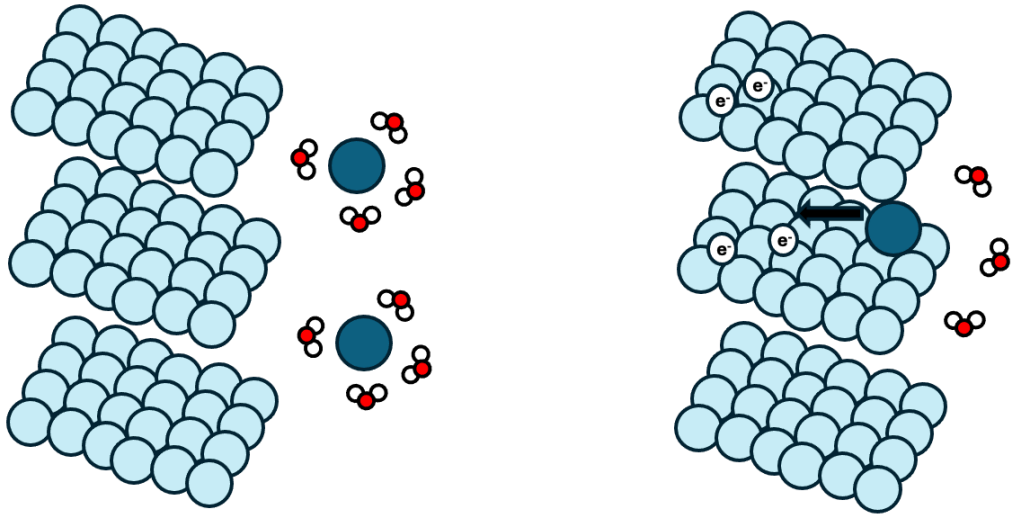

Figure 5: Schematic of proton-coupled electron transfer (PCET) process into a porous electrode. A solvated ion (left) approached the electrode interface and undergoes desolvation, where the water molecules are shed, and subsequently inserted into the electrode. Electrons travel through the solid electrode to meet with the inserted ion. Within this schematic, the water molecules are depicted to solvate a negatively charged anion, based on their orientation around the cation.

In many electrochemical systems, particularly those involving transition metal oxides, ion and electron transfers are not always independent events. Some ion transfer reactions are *concerted*, where an ion and electron complete a transfer conjunctively. When the ion involved in the concerted reaction is a proton, the term *proton-concerted electron transfer* (PCET) encompasses the phenomenon where both species transfer to each other in the same elementary step.[19] PCET can proceed through inner or outer sphere electron transfer via electron tunneling, and could have many steps, convoluting the understanding of kinetics in PCET processes.[19] In metal oxide insertion materials, these steps can be described in two phases referenced to a

cathodic process. The first phase, in Figure 5a, involves electron transfer from the current collector and through the electrode material to the redox material in solution, which often results in a change in the crystal lattice structure. The second phase involves the process of ion transfer to the electrode from solution, as seen in Figure 5b. In systems where the anion is the insertion material, insertion would happen when the electrode is positively charged, and the situation would be exactly reversed from what we could expect for cation intercalants. The ion must diffuse from bulk solution in response to a concentration gradient imposed by applied potential, then shed its solvation shell once it enters the vicinity of the electrode, then transfer into the electrode and diffuse through the electrode.[16] The role of ionic desolvation is believed to present a large portion of the energetic activation barrier but the specific mechanism is unclear. Chekshukin et al. used computational methods to investigate the rate of lithium ion desolvation in multiple solvent systems, which has a higher energetic effect in organic solvents than water.[23] It is unknown whether an aqueous desolvation barrier contributes significantly to PCET in transition metal oxides, particularly that of WO_3.

The kinetics of PCET are strongly influenced by environmental factors such as pH and the identity of the proton donor, both of which play critical roles in homogeneous and heterogeneous systems. Homogeneous inner-sphere PCET was studied by Lewis et al. to define kinetics in varied pH environments, where PCET in acidic conditions was fourfold faster than in basic conditions.[24] In heterogeneous PCET, the identity of the proton donor is highly prevalent for kinetic considerations, where the pKa and ability of the proton to interact with active surface sites. Jackson et al. investigated the effect of varying proton donation species in the electrolyte solution on the hydrogen evolution reaction (HER), and discovered that HER on gold was improved by having a phosphate anion as a mediator, which can compete with water as a proton

donor.[25] In the realm of electrocatalysis, it could be desirable to expedite the HER reaction or slow it, depending on the application, which makes proton-donor dependence an attractive area of study for fundamental electrochemistry. Despite its relevance, this type of proton donor investigation remains sparse in the literature for insertion materials, leaving a gap in our understanding of PCET mechanisms in these systems. Investigating the role of proton donors in insertion systems like tungsten oxide not only enhances our understanding of PCET kinetics but also helps identify how specific electrolyte components influence reaction rates. These insights are essential for rationally designing electrochemical interfaces that optimize ion transfer, for the ultimate goal of advancing technologies for a future of clean energy.

Chapter 1: Experimental Methods and Sample Preparation

Electrode Preparation

Fluorine-doped tin oxide (FTO) films on glass slides obtained from Sigma-Aldrich™ were used as conductive substrates and were prepared by cleaning in deionized water, then sonicated in acetone and isopropyl alcohol (99.8% Fisher Chemical) in the presence of ultrasonic waves via sonication. The slides were then plasma-cleaned in an O_2/N_2 gas mixture for 10 minutes to obtain a surface free of organic contaminants. Tungsten metal was sputtered onto masked FTO slides to 10 nanometers nominal thickness. An Ångstrom Instruments EvoVac sputterer with a base pressure of 10^{-6} Torr was used to deposit 0.5 Å of tungsten metal per second. The pure tungsten film was then thermally annealed in an oven under oxygen-flow for 24 hours to oxidize the tungsten into tungsten trioxide. The oven temperature was brought up to 425 °C at a ramp rate of 4.25 °C/minute.

FTO, a highly conductive substrate, was used to establish a back-contact with the WO_3 film because it is highly conductive. An exposed region of FTO on the edges of the electrode allowed the establishment of a conductive back-contact which reduced the overall resistance of the measurement. The thin film WO_3 electrode was used to minimize diffusional resistance of protons within the film and to ensure that electron transfer was not the rate determining step.

Figure 6: Side View of Tungsten Oxide Electrodes

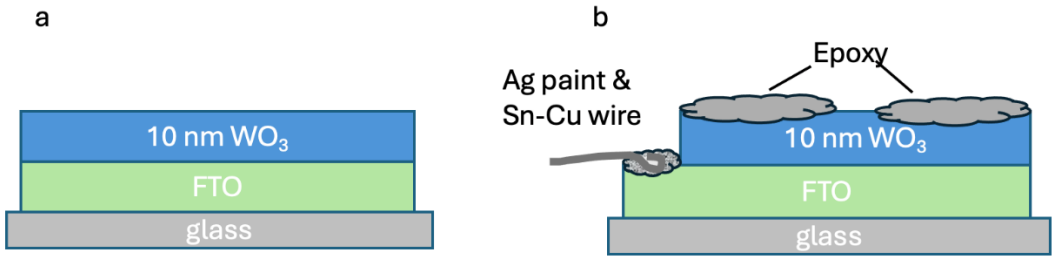

Figure 6: Side view of WO_3 electrode fabrication for a) the result directly after annealing the WO_3 under oxygen flow and b) the wire back-contact on the FTO open face done to decrease series resistance.

This oxidation turns the film from a metallic color to a translucent yellow film which turns translucent blue upon proton insertion. This color change is due to the altered HOMO-LUMO gap between bonding and anti-bonding orbitals when electrons are inserted and removed from the molecular bonding orbitals. Figure 6a shows the tungsten on FTO after sputter deposition and oxidation, and Figure 6b shows the final product of the manufactured electrode.

Figure 7: Electrode Fabrication Process for Tungsten Oxide Electrodes

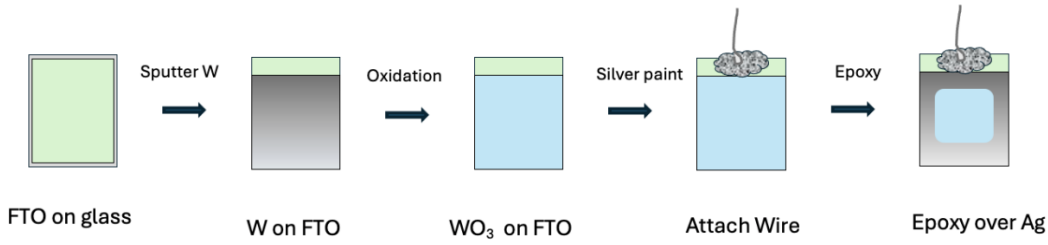

Figure 7: Electrode fabrication process for WO_3 thin films, where the Potentiostat wire is connected to the open FTO face after sputtering and oxidation.

Figure 7 shows the stepwise scheme for electrode fabrication. Tungsten slides are cut to the appropriate electrode size, approximately 1cm x 1cm. Tinned copper wire is attached to the bare FTO part of the electrode and connected with liquid silver paint. Tinned copper wire is used

for its immense conductivity and oxidation/degradation resistance. Once the paint is dried, the Cu wire is further connected with acid-stable epoxy. The epoxy must cover the entirety of the tinned-copper wire and silver paint to mitigate any side reactions. The epoxy is painted over the entire surface of the WO_3 electrode, leaving a square window of WO_3 visible, thereby deemed the 'active area' for proton insertion. The epoxy is smoothed to the smallest thickness, so the flow of liquid is not interrupted by a physical barrier. A cleaned glass tube is placed over the tinned copper wire and secured with epoxy, so it never comes into contact with the electrolyte solution in the cell.

A pure platinum counter electrode was made by soldering platinum to a larger tinned copper wire. A glass tube protects the pristine solution from the solder or tinned copper wire from contamination. A silver/silver chloride (Ag/AgCl) reference electrode is used to measure the voltage against a well-specified reference point. A jacketed three-necked round bottom flask was used to contain the three-electrode cell and control the temperature (Figure 8). The outer jacket was connected to a recirculating chiller, which circulated an insulating mixture of propylene glycol and water to maintain a constant heat within the cell.

Figure 8: Three-Electrode Cell Schematic

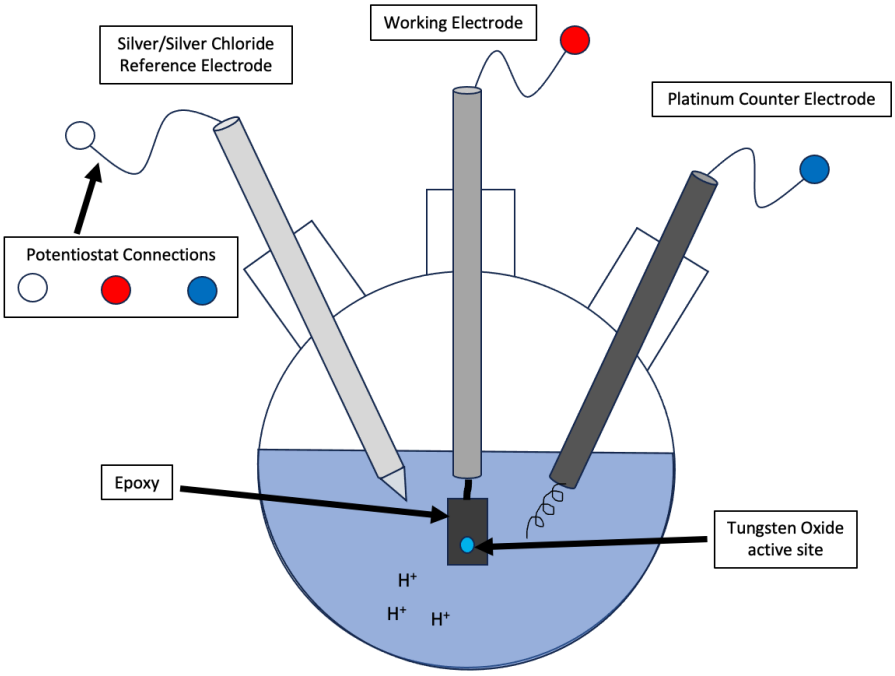

Figure 8: A three-necked round bottom flask was chosen as the three-electrode cell for close proximity of the electrodes and proper temperature control with jacketing (jacket not shown). Each electrode is connected by a metal clip to the Potentiostat to make the electrochemical measurements, where the white connection is the Ag/AgCl reference electrode, the red connection is the WO_3 thin film working electrode, and the blue connection is the Pt wire counter electrode.

Solution Preparation

Control measurements were made in an electrolyte solution of 1M HCl so only one proton donor is possible for proton insertion. Additional solutions were made with the intent to vary the concentration of a single source of proton donor while holding the others constant. A potassium sulfate buffer solution was crafted by titrating sulfuric acid with potassium hydroxide until the pH was equal to the pKa of the HSO_4^-/SO_4^{2-} ratio. In this way, the Henderson-Hasselbach equation (Equation 5) for buffer solutions was satisfied. Then, a dihydrogen

phosphate buffer ($H_2PO_4^-/H_3PO_4$) with a pKa of 2.15 was made in the same manner to compare two electrolyte systems.

$$pH = pKa + \log\left(\frac{[A^-]}{[HA]}\right) \quad [5]$$

This varied the ratio of buffer proton donor to hydronium in solution. Potassium chloride (KCl) supporting electrolyte was added in these instances to mitigate migration in the bulk electrolyte, establish a constant capacitance at the electrode surface, and maintain a high solution conductivity to reduce series resistance. All aqueous solutions were prepared with 18.2 MΩ cm^{-1} Ultrapure deionized water using volumetric flasks to obtain a precisely known concentration.

$$x\mathrm{HSO_4^-} + \mathrm{WO_3} \rightarrow \mathrm{H}_x\mathrm{WO_3} + \mathrm{SO_4^{2-}} \quad [6]$$

Figure 9: Bisulfate Proton Donor Schematic

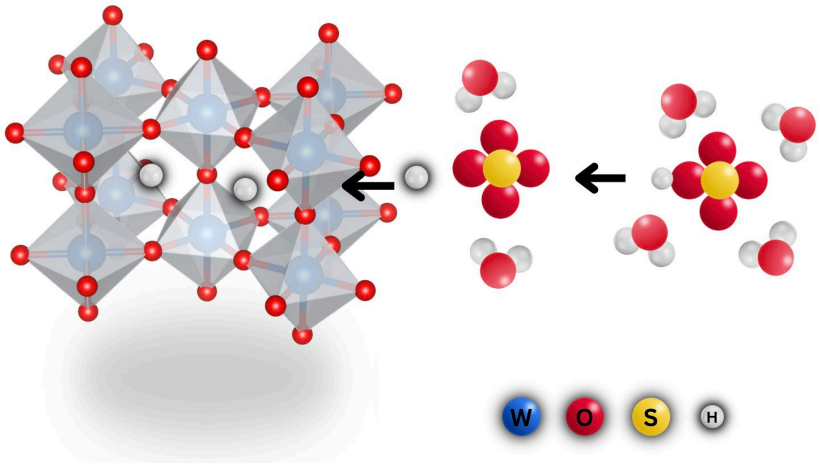

Figure 9: Possible reaction scheme of proton donation done by the bisulfate anion, where the anion is initially solvated by surrounding water molecules in aqueous solution, then desolvated before the proton is intercalated into the WO_3 electrode.

$$x\mathrm{H_2PO_4^-} + \mathrm{WO_3} \rightarrow \mathrm{H}_x\mathrm{WO_3} + \mathrm{HPO_4^{2-}} \quad [7]$$

Figure 10: Dihydrogen Phosphate Donor Schematic

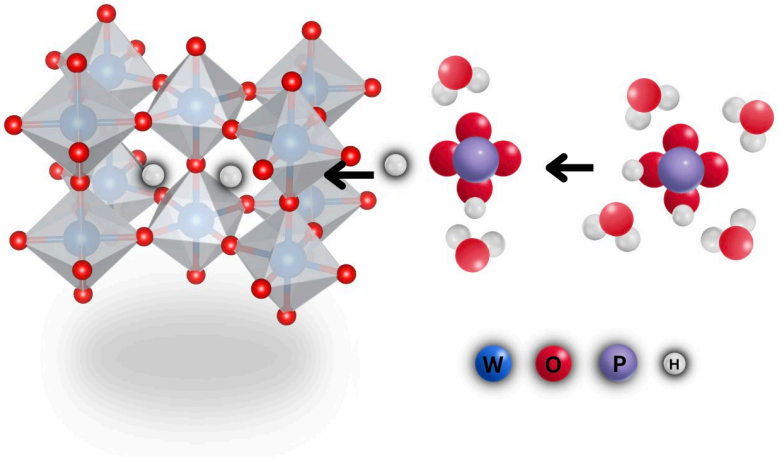

Figure 10: Possible reaction scheme of proton donation done by the dihydrogen phosphate anion, where the anion is initially solvated by surrounding water molecules in aqueous solution, then desolvated before the proton is intercalated into the WO_3 electrode.

Systematic changes to the concentration of buffer in solution while maintaining a constant concentration of hydronium ions in solution allowed the kinetics of proton donation to WO_3 to be evaluated.

It is expected that a larger concentration of buffer will enable faster rates of transfer if the buffer is indeed the proton donor. The theoretical reaction mechanisms in Figures 9 and 10 show the proton donation sequence if the selected buffers are proton donors, while Equations 6 and 7 correspond to the reactions. The results from the kinetic analysis of buffer proton donors will be further discussed in Chapter 3.

Potentiostat

Figure 11: Bio-Logic Potentiostat

Figure 11: SP-200 Potentiostat with a low-current channel used for high resolution in all electrochemical measurements. Picture Courtesy of BioLogic. https://www.biologic.net/products/sp-300/.

A SP-200 BioLogic Potentiostat (Figure 11) with a low-current channel was used to make electrochemical measurements. Potentiostatic techniques were used to induce small

voltage changes in the system and observe the current output. EC-Lab software was used to perpetuate the measurements, and in certain cases, EC-Lab Express was used to obtain high-resolution current transient measurements. Cyclic voltammetry (CV) was used to measure a 'fingerprint' of the relevant reduction-oxidation reactions occurring at the tungsten oxide electrode surface. Potentiostatic Electrochemical Impedance Spectroscopy (PEIS) was used to observe the series resistance of the system. Chronoamperometry (CA) was used to instantaneously change the voltage and observe the system's effort to re-equilibrate.

Data Work-Up

Python programming software, Jupyterlab, was used for all data analysis and work-up. Limfit and SciPy packages were used to write a script for current transient and Butler-Volmer fitting, respectively. Some code was developed with the assistance of Nicholas D'Antona.

Chapter 2: Electrochemical Methods – A Guide to Data Interpretation

Cyclic Voltammetry

Cyclic voltammetry (CV) is a robust electrochemical technique used to extract a "fingerprint" of the redox activity and relate the relative reaction rates to an electron transfer process. Cyclic voltammetry applies a linearly increasing potential while measuring the resulting current output at the working electrode. The x-axis, potential (V, J/C), controls of the driving force applied to the reactions, which effectively changes the energy level of the electrons within the electrode. Potential differences are always measured against a highly reversible and stable reaction, here Ag/AgCl. For this aqueous system, an Ag/AgCl reference is used because the reactions of interest are within the operating potential window of the reference electrode. Furthermore, the y-axis is current (A, C/s), which indicates the rate of electrochemical reaction. The rate at which potential is increased is called a scan rate in mV/s, wand can be changed to modulate relative reaction rates.

When a potential is applied to the electrode to cause a surface electrochemical reaction, a concentration gradient develops between the electrode surface and bulk solution, prompting the diffusion of species towards the electrode. This diffusion layer grows with time, causing a peak in the CV scan when mass transport limitations are reached. Under these limitations, the current is limited by the number of species available to travel to the surface. Furthermore, an increased scan rate creates a larger extent of reaction at the electrode surface by promoting an increased concentration gradient, causing a higher current response in the scan.

Figure 12: A Cyclic Voltammogram of Proton Insertion into WO_3

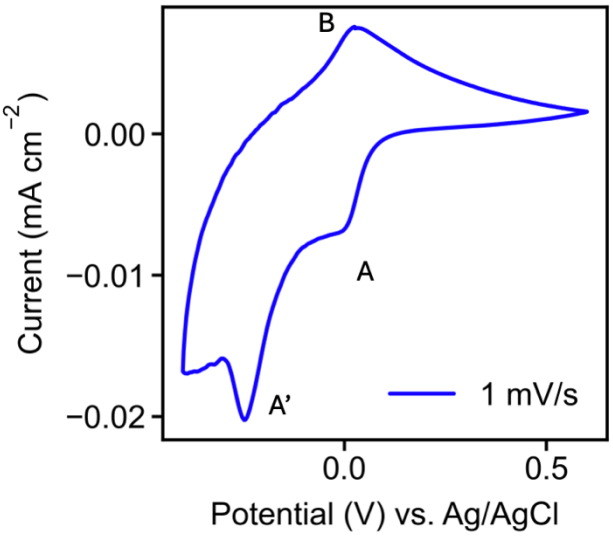

Figure 12: A cyclic voltammogram of the WO_3 thin film in 1M HCl at 1 mV/s scanned from -0.6 V to 0.6 V vs. Ag/AgCl. There are two prominent insertion peaks on the cathodic sweep, A and A', showing the two phases of proton insertion. Then, on the anodic potential sweep, only one proton de-insertion peak at B is seen.

A CV of tungsten oxide is seen in Figure 12, where there are two distinct peaks for both reduction and oxidation phenomena. As the potential sweeps from positive to negative voltages, a reduction reaction occurs at the electrode, where protons in solution are inserted into the WO_3 lattice. Here, electrons travel through the WO_3 substrate via quantum tunneling, until they reach a proton in the reduction reaction. Then, on potential sweeps from negative to positive voltages, an oxidation reaction occurs where the hydrogen atoms are expelled from the WO_3 lattice and back into solution.

The appearance of two redox peaks indicates a multi-step reaction for proton insertion. However, the exact mechanism of this reaction is unknown. It can be speculated that a phase transition within the WO_3 occurs to better accommodate the additional nucleus within the lattice. On the cathodic sweep in the CV, two notable peaks at A and A' form, indicating the proton

insertion occurring in two mechanistic steps. Then, on the anodic sweep, there is only one de-insertion peak. This indicates that there is some extent of irreversibility within the system, further affirmed by the peak separation potential between B and B'. Furthermore, in Figure 12, there is increased capacitive current accompanying faradaic processes, which can be attributed to the pseudocapacitive contribution of proton adsorption and desorption. The peaks do not mirror each other for the anodic and cathodic regions, implying some degree of irreversibility within the system. Furthermore, when multiple cycles are taken, there is no observed degradation in the current for anodic or cathodic reactions.

If the potential window were extended to more cathodic (negative) overpotentials, the hydrogen evolution reaction (HER) will occur past bulk proton insertion. Miu et al. showed that bulk proton insertion must happen within WO_3 before HER can occur.[15] This explains the 'tail' seen after peak A' in Figure 12. The electrolyte for the cell in Figure 12 was HCl, which provides only one proton donor source and therefore no source of proton donor competition is present in the CV. The effect of differing electrolyte solutions will be further studied by utilizing buffered electrolytes to vary the concentration of possible proton donors relative to each other. Future experiments could utilize spectroscopy measurements like X-Ray Diffraction (XRD) to analyze the extent of insertion and connect it to the structural changes within the film. A discussion about the different features of CV scans in buffered proton donor systems will be addressed in Chapter 3.

Electrochemical Impedance Spectroscopy

Another electrochemical technique critical to this experiment was electrochemical impedance spectroscopy (EIS), used to extract the resistances of each electrode. Resistance has a

profound effect on the entire electrochemical circuit, and each measurement must be corrected to account for the resulting potential drop. Ohm's Law, in Equation 7, describes the linear relationship between voltage and the product of current and resistance. "iR" drop is termed to represent the loss in potential due to the existing resistance within the system. In a model system, it is imperative to maintain a low resistance so the reaction driving force is devoted entirely to the electrochemical reaction rather than extraneous sources. "iR correction" is the mathematical correction used to account for the loss in driving force of potential due to this resistance, in Equation 8.

$$V = iR \text{ [7]}$$

$$E = E_{applied} - iR_{series} \text{ [8]}$$

An EIS measurement is taken by applying an input sinusoidal wave over a range of frequencies and measuring the phase and amplitude of the output sinusoid.[26] The output of EIS used in this study is a Nyquist plot, which plots the negative imaginary impedance versus the real impedance. Impedance is the opposition of current flow, which can be caused by many different phenomena, like capacitance, resistance, inductance, or diffusion effects. The discrepancy between the input and output sinusoid of phase is depicted on the imaginary axis while the amplitude is depicted on the real axis. The phase is generated by the relative magnitudes of the real and imaginary impedances, yielding information about the relative sizes of these impedance components.

Figure 13: Circuit Diagram of a Randle's Circuit

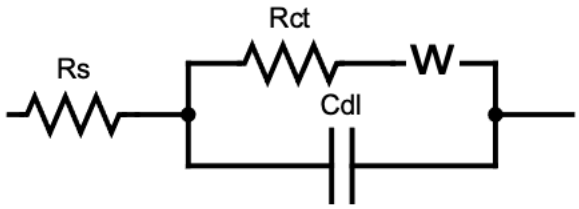

Figure 13: Circuit diagram of a Randle's circuit, where R_s is the series resistance, R_{ct} is the charge transfer resistance, W is the Warburg element for diffusion, and C_{dl} is the double layer capacitance. The corresponding Nyquist plot can be found in Figure 14a.

The behavior of Nyquist plots reflects the equivalent circuit elements pertaining to a system. The Nyquist plot data was fit to a Randle's equivalent circuit to predict the contributions of resistance, capacitance, and diffusion effects to the impedance of the three-electrode cell system. A Randle's circuit describes a resistor in series with a parallel RC circuit, with an additional component called a Warburg element. Figure 13 shows the Randle's circuit diagram and modeled data from such a circuit. The Randle's circuit resistors represent the solution and charge transfer resistances, while the capacitor represents the double-layer charging phenomena. The Warburg element represents the impedance caused by diffusion at low frequencies and longer time scales. While impedance from resistors and capacitors show up at high frequencies in this measurement, the Warburg element shows up as a linear and angled feature in a Nyquist plot.

Figure 14: EIS Data Simulated and Fitted to a Randle's Circuit

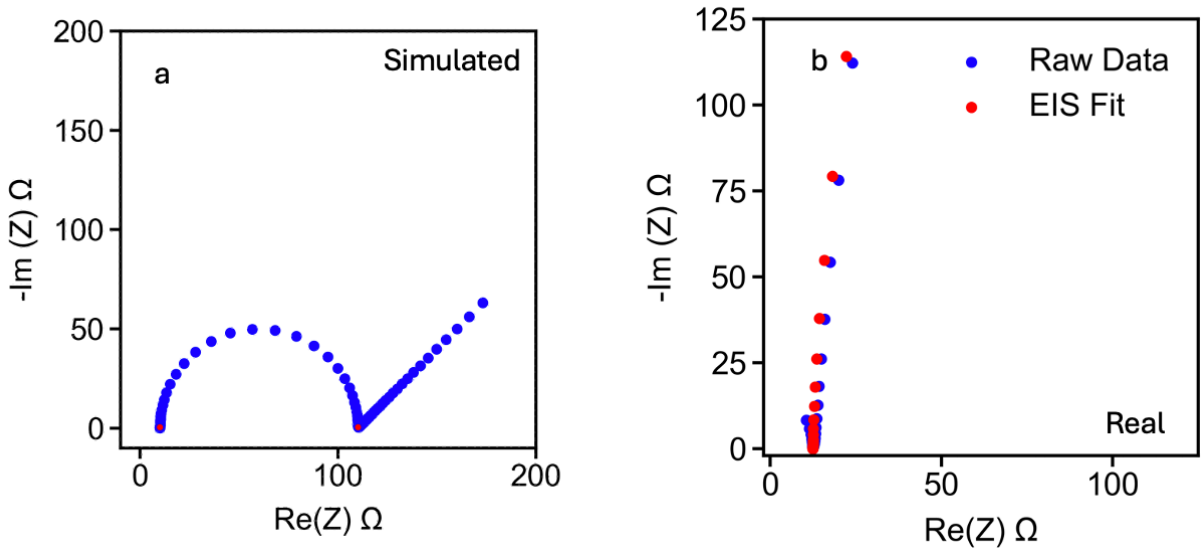

Figure 14: EIS measurements depicting the difference between (a) the simulated ideal equivalent Randle's circuit (Rs = 10 Ω, R_{ct} = 100 Ω, and C_{dl} = 10-6 F) and (b) a real WO_3 thin-film electrode measurement, where the blue scatter is the raw data while the red scatter is the EIS fit to a Randle's circuit, with fitting results: Rs = 12.46 Ω, C_{dl} = 5.94 * 10-5 F, R_{ct} = 3.64 * 10-4 Ω.

The Nyquist plots produced from WO_3 electrodes (Figure 14b) often lacked the characteristic semi-circle of the Randle's equivalent circuit in Figure 14a. Instead, PEIS scans showed an intersection with the x-axis, where the series resistance of the cell was extracted, and then a linear increase, consistent with a capacitive or diffusion-controlled phenomenon at the electrode surface. The diffusion-limited feature in the EIS is likely not from proton diffusion within the film because thin films were used to avoid this limitation. By making the electrodes extremely thin, there are only a few unit cells of the lattice on the electrode, so there is a smaller distance for the solid-state diffusion layer to exist in. Instead, the system becomes diffusion limited from solution as protons nearby the electrode are depleted at a constant voltage hold. The rapid upward increase in negative imaginary impedance is also consistent with a circuit controlled by a small capacitance, which could relate to the pseudo-capacitive phenomena observed in the cyclic voltammogram.

Figure 15: Potential-Dependent PEIS of Tungsten Oxide

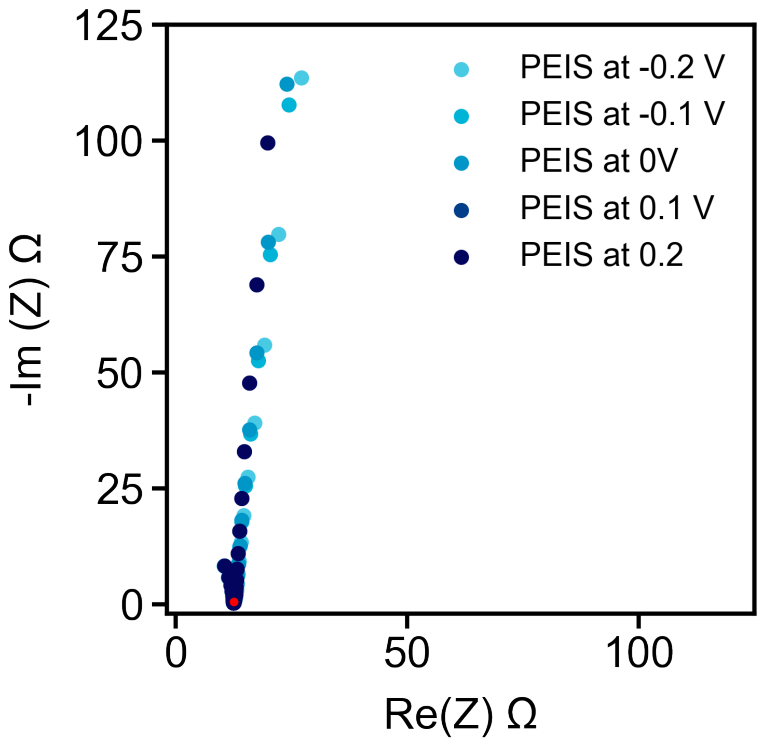

Figure 15: PEIS scans of the WO_3 thin-film electrode for various overpotentials versus an Ag/AgCl reference electrode, showing consistency in series resistance among applied overpotentials.

The potential applied to the system prior to applying the sinusoidal frequency did not affect the outcome of the EIS scan (Figure 15). While it is known that the conductivity of WO_3 increases as protons are inserted, this did not have a significant impact on the total series resistance. The series resistance for any given WO_3 electrode was constant across applied voltages and therefore made *iR* correction more consistent.

Chronoamperometry

Chronoamperometry, the measurement of a current transient, was used to reveal important kinetic information about the WO_3 model system.

A chronoamperomogram (CA) begins with a stepwise change to the potential at the working electrode and records the resulting current response. In the following experiments, the potential was held for 1 minute at a stable "poise" potential to create a quasi-equilibrated state at the electrode surface. Then, the potential was stepped in increments positive and negative from the equilibrium potential and the current response is observed. The increase in magnitude of the potential step (a) corresponds to an increase in current response (b) (Figure 16). Additionally, the initial current response rapidly decays until the asymptote approaches zero current in Figure 16b. For the following study, a "poise" potential of -0.3 V was chosen, as it was observed to be centered within the realm of bulk proton insertion. Bulk proton insertion describes the region in the CV (Figure 16a) before the onset of HER at cathodic overpotentials, but after the initial reduction feature of proton insertion at -0.15 V. With this "poise" potential, the chronoamperometry measurements span a potential range over both A and A' redox features.

Figure 16: Current Transient Measurements

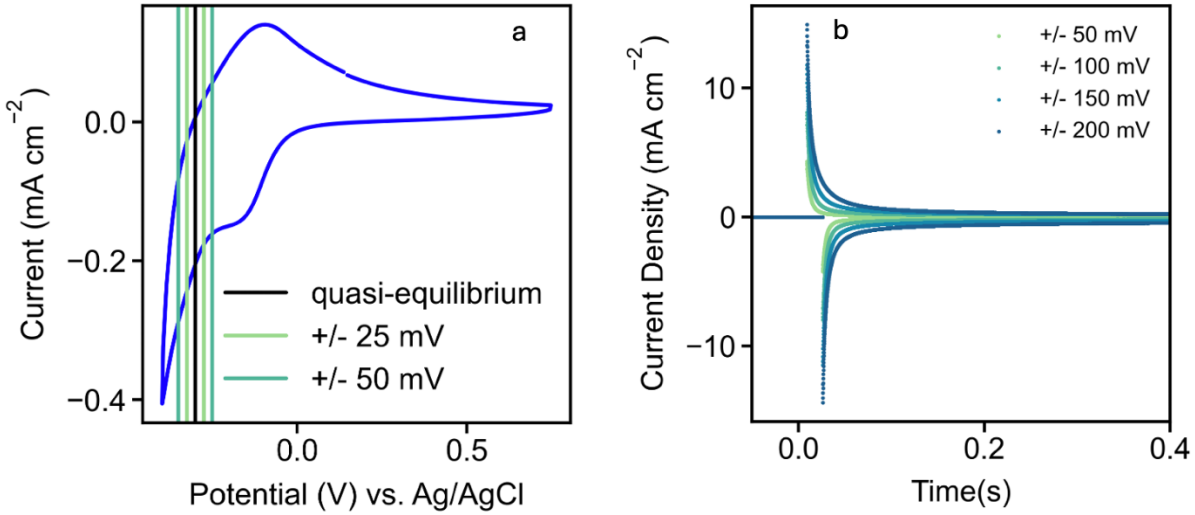

Figure 16: The schematics of a current transient measurement are shown by a) a CV of WO_3 in 1 M HCl at 100 mV/s, where the vertical lines correspond to magnitudes of change in the potential from the quasi-equilibrium potential of -0.3V vs. Ag/AgCl and b) the resulting current response versus time which shows an increasing magnitude of current for each corresponding potential jumps.

Each CA provides a wealth of information about reaction kinetics that must be extracted through distinguishing between interfacial processes. As previously mentioned, ion transfer and double-layer charging occur simultaneously at the electrode-electrolyte interface, and both contribute their respective current to the CA measurement. A model equation, Equation 9, for the resultant CA current was devised to separate the respective reaction currents to isolate the ion transfer current. Here, the first exponential term modifies the exponential decay of current from double layer charging, where A signifies the double-layer charging coefficient, t is time, and c is the RC time constant. The second term is a double-exponential fit for ionic transfer current, where B signifies the maximum ionic transfer current, τ_{PT} signifies the proton transfer time constant, and y is an intercept to adjust the y-axis position.

$$j(t) = Ae^{-\frac{t}{\tau_{RC}}} + B\left(1 - e^{-\frac{t}{\tau_{RC}}}\right)e^{-\frac{t}{\tau_{PT}}} + y \text{ [9]}$$

This equation, based on the assumption that the rate of reaction is proportional to the time dependent potential difference established at the electrode interface, provided a satisfactory fit for the current transient data (Figure 17). Here, the green trace signifies the exponentially decaying double later charging while the red trace signifies the ion transfer current. The ion transfer current is assumed to rise and fall with a function of time. The rise in current is due to the competition with double-layer charging, as well as overcoming the energetic activation barriers of the proton transfer reaction. The rapid decline in ion transfer current is attributed to the growing diffusion layer at later times. When these fit curves are added up to yield the total fit equation, there is adequate overlap between the equation and real data with low residuals. Since we do not expect the time constant for the double layer charging (τ_{RC}) to vary substantially with the applied potential, a global fit for the RC time constant was imposed for one set of current transients. One set of current transients is all of the potential steps from one equilibrium potential for the same electrode and same electrolyte concentration. This assumption was justified by the fact that the series resistance was observed to persist at a constant value across overpotentials, and the ionic strength is maintained across experiments to reduce variance in capacitance.

Figure 17: Fitted Current Transient Measurement

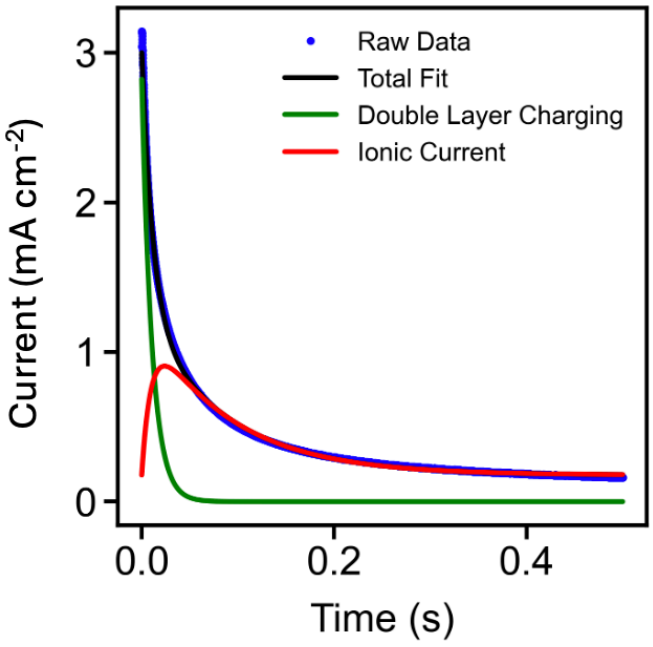

Figure 17: The resulting fit curve from the Equation 9, where double layer charging current (green) and ionic transfer current (red) combine to produce a total fit line (black), which fits well to the raw data curve (blue).

Butler-Volmer Kinetic Analysis

$$j = j_0\left(e^{\frac{(1-\alpha)zF\eta}{RT}} - e^{\frac{(-\alpha)zF\eta}{RT}}\right) [10]$$

Finally, after the current transient measurements were fitted, the data can be used to extract kinetic parameters from the Butler-Volmer equation (Equation 10). The Butler Volmer equation posits that the current response (j) from increasing overpotential (η) will be exponential and fits this response for both cathodic and anodic reactions. Other parameters in the Butler-Volmer equation include the charge transfer coefficients, α, R as the ideal gas constant, T as the temperature of the measurement, and z as the number of electrons transferred. Using the B values from the current transient fitting, the maximum ionic current was plotted against the

overpotential and fitted to Equation 10. Here, j_0 signifies the exchange current density, which is a valuable kinetic parameter describing the intrinsic activity of the electrode. The more kinetically facile the reaction is, the higher the j_0 parameter will be. The charge transfer coefficients signify the energetic symmetry of the reaction, where the first term with 1- α is the anodic reaction and the -α term is the cathodic reaction. When alpha is 0.5, the reaction is perfectly symmetrical and both cathodic and anodic reactions are equally probable. When the value of alpha deviates from 0.5, the current of one-half reaction will increase while decreasing that of the other.

$$j = j_0 \left(e^{\frac{(\beta) z F \eta}{RT}} - e^{\frac{(-\alpha) z F \eta}{RT}} \right) [11]$$

This deviation from a symmetric charge transfer coefficient was found to occur in every Butler-Volmer fitting. Therefore, this system did not follow a symmetric charge transfer energetic barrier, so we needed to separate the charge transfer coefficients for both anodic and cathodic components. To account for this, an extra fitting parameter, β, was used to replace 1- α, as seen in Equation 11. In Figure 18, this modification is shown in teal and compared to the regular Butler-Volmer fit. The data shows a less steep increase in both anodic and cathodic directions than predicted by the Butler-Volmer equation.

Figure 18: Butler-Volmer Fitting

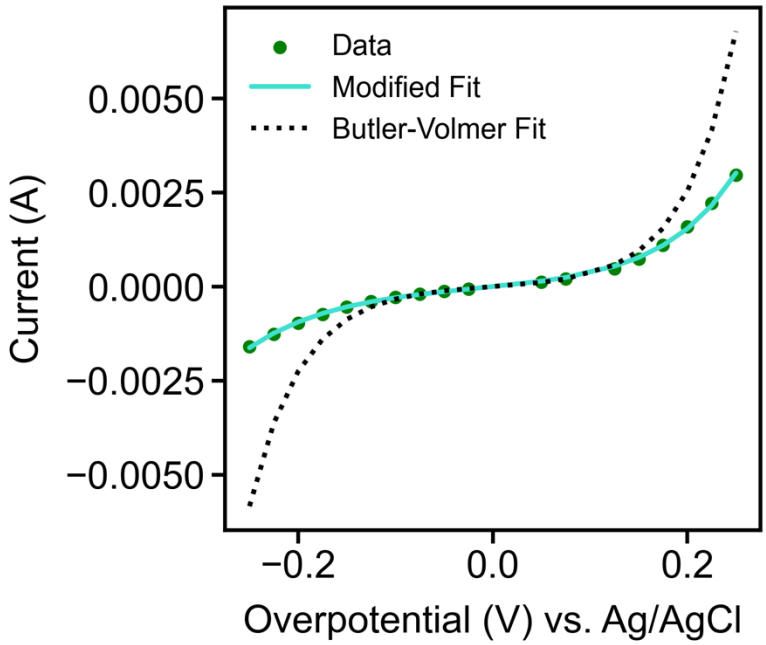

Figure 18: Butler-Volmer data obtained from the current transient fitting method in green, where the data was fitted to the Butler-Volmer equation (in black dotted line), and furthermore, the data was fitted to the modified BV equation in teal. This BV curve has been iR corrected for the series resistance of the electrode.

This extra fitting parameter indicates a non-ideality in the charge transfer relationship, where some potential applied to the system is going towards a process other than ion insertion. Since the current transient fitting method accounts for the double-layer charging of the electrode, every Butler-Volmer curve is iR-corrected for the series resistance, other phenomena could be causing the non-ideality of charge transfer coefficients. For example, a phase transition, also indicated by the multiple redox peaks in the CVs, could be raising the transition energy barrier for proton insertion, causing additional potential to be directed towards that aspect of the reaction. Additionally, surface adsorption or desolvation could be contributing to the charge transfer energetic barrier.

Chapter 3: Results and Discussion of Buffer Strength Alteration

Proton Insertion in Dihydrogen Phosphate Buffer

Two buffer strengths (10 mM and 100 mM) of the potassium dihydrogen phosphate buffer (pKa = 2.15) were tested for their proton insertion kinetics with the aim of identifying the most favorable proton donor species in solution. For this buffer system, there were three possible proton donors in solution: H_2O, H_3O^+ , or $H_2PO_4^-$, as illustrated by Figure 10. The experimental analysis made for the potassium bisulfate donor was repeated for the potassium dihydrogen phosphate, including comparisons of cyclic voltammetry, Butler-Volmer curves, and exchange current densities. Previous studied on a gold rotating disk electrode (a non-porous electrode) showed that this biphosphate buffer enhanced the kinetic activity of HER, so this buffer was of interest in the proton insertion reaction.[25]

Figure 23: Scan-Rate Dependent Cyclic Voltammetry in Phosphoric Acid Buffer

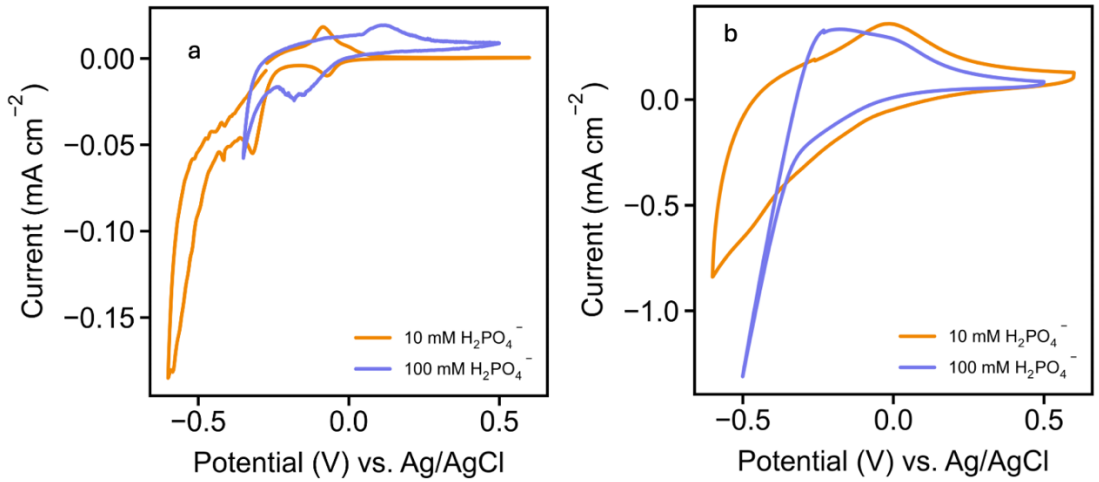

Figure 23: Cyclic voltammetry scans at a) 1 mV/s and b) 100 mV/s in 10 mM (orange) and 100 mM (purple) for the same WO_3 electrode, where current is normalized to the area of the electrode.

Figure 23 indicates the effect of dihydrogen phosphate buffer concentration on the cyclic voltammetry profile for multiple scan rates. At 1 mV/s, there is a higher resolution of the redox peaks in Figure 23a than at 100 mV/s in Figure 23b, due to the additional time allowed for the reaction to equilibrate at slower scan rates. The cathodic features for the 10 mM $H_2PO_4^-$ show two peaks instead of only one observed for the 100 mM $H_2PO_4^-$. Additionally, the 100 mM $H_2PO_4^-$ CV in Figure 23a shows a positively shifted peak, indicating a more favorable redox reaction in higher dihydrogen phosphate concentration due to less required applied overpotential. It is significant that the hydrogen evolution reaction (HER) is shifted by several hundred mV for a higher concentration of dihydrogen phosphate, which was previously observed on a gold surface.[25] In Figure 23b, HER onset also occurs at significantly less overpotential for 100 mM $H_2PO_4^-$ than 10 mM $H_2PO_4^-$. Furthermore, the redox peaks at higher scan rates are different, where the cathodic peaks A and A' are not observed.

Figure 24: Cycle-Dependent Current Decay in Dihydrogen Phosphate Buffer

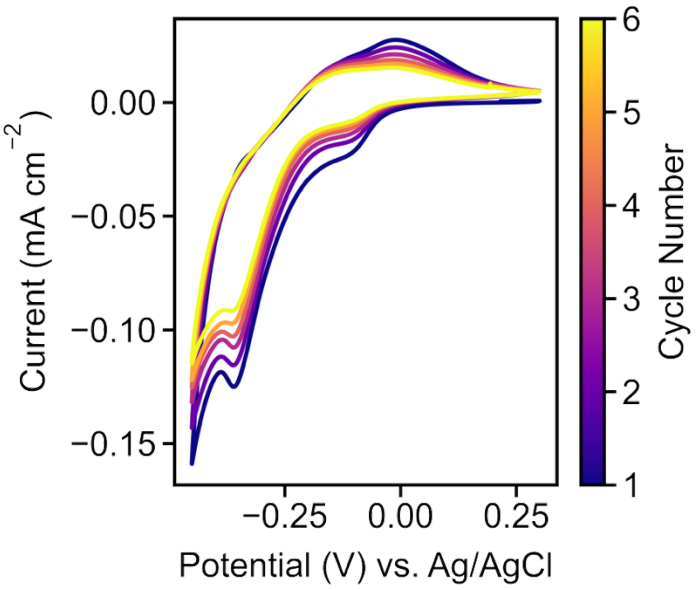

Figure 24: This CV of one electrode in 10 mM dihydrogen phosphate buffer shows the effect pf multiple cycles on the current. The current is seen decreasing in both the anodic and cathodic regions as the cycle number increases.

The change in redox features as a result of electrode cycling in 10 mM $H_2PO_4^-$ was highlighted in Figure 24. In other solutions, like HCl, H_2SO_4, and even HSO_4^- buffer, the decay of current was not observed as a function of cycling. However, Figure 24 clearly indicates a decrease in both anodic and cathodic redox features as cycle number increases, signifying a decreased retention of proton intercalants in the WO_3 lattice. The underlying cause of this behavior remains unknown, but it could be speculated that the phosphate anion may interact with the electrode surface more strongly, inhibiting reversible proton insertion and promoting surface reactions like HER. It remains that the overpotential of HER is less in the dihydrogen phosphate buffer than that of the potassium bisulfate buffer.

Figure 25: Potassium Dihydrogen Phosphate Buffer Butler-Volmer Curves

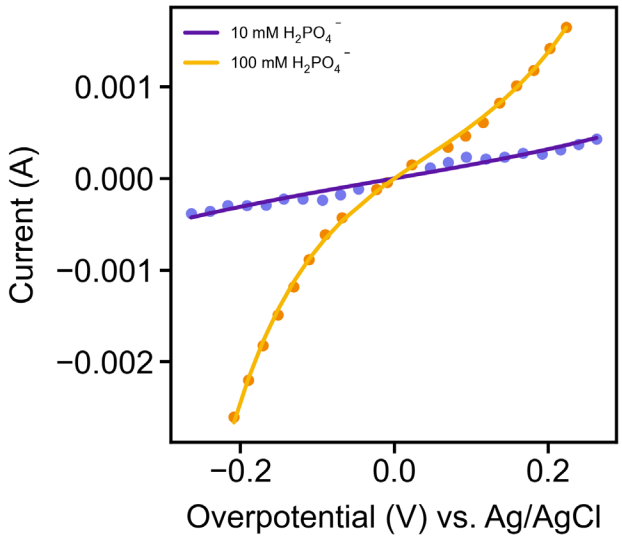

Figure 25: Butler-Volmer Curves for a single electrode in increasing dihydrogen phosphate buffer concentrations, showing distinct differences in current response for the 10 mM and 100 mM concentration of hydrogen phosphate proton donor. These preliminary results have not been repeated yet. The BV curves have not been iR corrected for their series resistance relative to the electrode and the varying electrolyte solutions.

The Butler-Volmer data extraction was repeated with the dihydrogen phosphate buffer to reveal significant changed in current with overpotential between concentrations of buffer in Figure 25. Preliminary results show that a higher concentration (100 mM) of phosphoric buffer prompted a higher current response compared to the lower concentration (10 mM). However, The Butler-Volmer fit for the 10 mM concentration was sub-optimal and exhibited high residuals, which could be due to a dysfunctional electrode.

Figure 26: Exchange Current Density in Phosphoric Acid Buffer

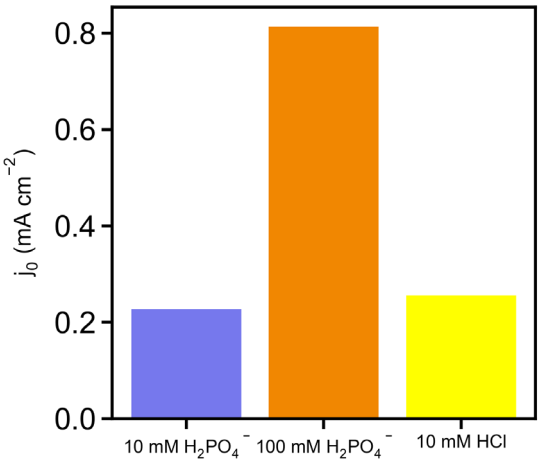

Figure 26: Bar graphs indicating the exchange current density for changing concentrations of dihydrogen phosphate buffer at pKa = 2.15, stemming from the Butler-Volmer fitting current transients. There are no error bars due to lack of repetition of the experiment. The 10 mM HCl exchange current is again compared to the exchange currents of proton insertion in buffered dihydrogen phosphate, where preliminary results show an increase in reaction kinetics for increasing buffer concentration.

From the Butler-Volmer fitting in Figure 25, the exchange current densities were extracted and plotted in Figure 26 as a function of concentration of proton donor species. The exchange current density of 100 mM $H_2PO_4^-$ was found to be significantly higher than that of the 10 mM concentrations of both $H_2PO_4^-$ and HCl. The Butler-Volmer fit was also adequate for this electrode, providing a dimension of reliability for the data. Preliminary results suggest that the phosphoric acid buffer could promote proton donation into the WO_3 lattice, a result that contrasts that of the bisulfate buffer solution. However, it was also observed that there were elevated rates of HER on the surface, which could have interfered with the measurement of ion insertion current. If this were the case, HER and ion transfer yielded convoluted current responses, and were not accounted for with this method.

While these results show an increase in exchange current density for the higher concentration of dihydrogen phosphate, the Butler-Volmer curves were not able to be iR-

corrected. This is due to the extremely large series resistances observed in each EIS measurement. While the potential dependence of the impedance response was explored with PEIS, most electrodes exhibited consistently high resistances at varied overpotentials. It is not understood why this phosphate electrolyte induces such a high impedance, while other electrolytes tested did not. It is hypothesized that there is a surface adsorption phenomenon, prevalent for higher concentrations of phosphate, which may inhibit proton insertion but increase HER. Since this system exhibited non-ideal behavior to study the model system of proton insertion, the proton insertion kinetics were studied in a potassium bisulfate buffer. The following system with bisulfate electrolyte exhibited less convoluted surface interactions, as seen in the electrochemical response, therefore making the data collection more suitable for sensitive ion transfer measurements.

Proton Insertion in Potassium Bisulfate

Three buffer strengths (10 mM, 100 mM, and 500 mM) of the potassium bisulfate buffer were tested for their proton insertion kinetics in the aim of identifying the most favorable proton donor species in solution. For this buffer system, there were three possible proton donors in solution: H_2O, H_3O^+ , or $HSO4^-$. It was hypothesized that the hydronium ion would preferentially donate its proton and outcompete the bisulfate ion because hydronium is a stronger acid. As hydronium has a lower pKa than that of bisulfate, it has a higher intrinsic ability to expel its proton and retain molecular stability after the donation. The concentration of the proton donor, detected by the resulting current, was expected to be indicative of the proton donor.

Figure 19: Cyclic Voltammetry of Various Bisulfate Concentrations

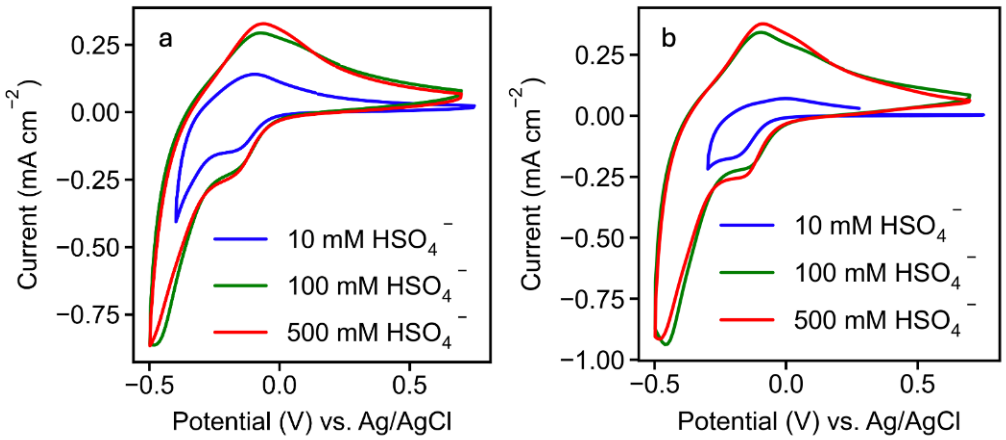

Figure 19: Cyclic voltammetry scans at 100 mV/s at various concentrations of the potassium bisulfate buffer solution for two different WO_3 electrodes (a & b), where the current is normalized to the area of the electrodes. There are differences in current between the 10 mM HSO4- and the two higher concentrations, 100 mM and 500 mM HSO4-, suggesting a lower activity in the electrode for the lower concentration solution. The CVs have been iR corrected with a series resistance specific to their electrode and electrolyte solution.

Figure 19 shows the CV scans at 100 mV/s for the same WO_3 electrode in different buffered proton donor concentrations. Here, Figure 19a is one WO_3 electrode and Figure 19b is a different electrode, shown to highlight the reproducibility of these trials in potassium bisulfate. The scan rate was held constant across CVs of each concentration at 100 mV/s. It is noteworthy that the current response increased after the 10 mM bisulfate buffer CV and was consistent for the 100- and 500-mM bisulfate buffer. Since the ionic strength was held constant, the double layer charging contributions to current are expected to be constant across solutions. These findings indicate that the change in concentration of electrolyte may be responsible for the change in current response of the CV. This effect of increased current was explored by the following kinetic analysis.

Figure 20: Potassium Bisulfate Buffer Butler-Volmer Curves

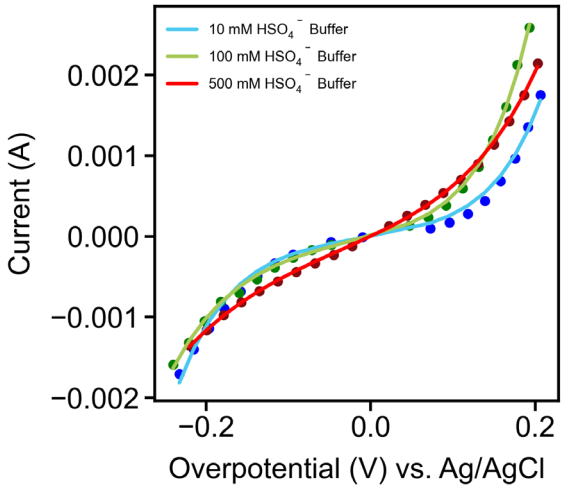

Figure 20: Butler-Volmer Curves for a single electrode in increasing bisulfate buffer concentrations, showing no significant change in current response with additional overpotential applied to the system. The BV curves have been iR corrected for their series resistance relative to the electrode and the varying electrolyte solutions.

The current transient method for measuring proton insertion kinetics, described in Chapter 2, was used to form Butler-Volmer curves in varying bisulfate concentration, as seen in Figure 20. Each data set had small residuals, indicating a good fit of Butler-Volmer equation, and therefore confirming that this equation is justified as a kinetic model for proton insertion. There are minimal changes in the shape of the curve and magnitude of the current response to overpotential across different concentrations of potassium bisulfate buffer. This suggests that the concentration of bisulfate in solution did not appreciably impact the intrinsic reaction rate.

Figure 21: Exchange Current Density Results for Varying Bisulfate Concentrations

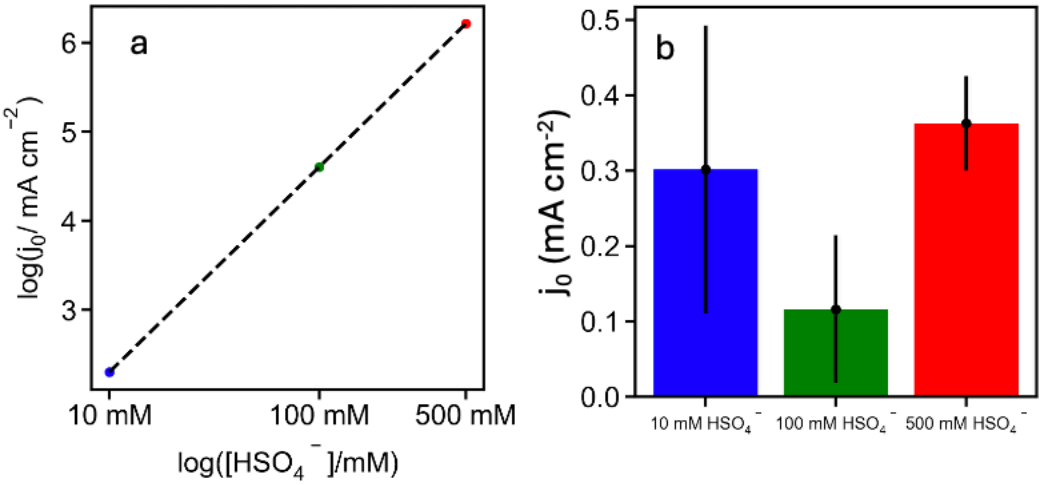

Figure 21: Graphs indicating the exchange current density for changing concentrations where a) represents the expected increase in exchange current density if the reaction followed a first order kinetic rate law based on the dependence of bisulfate concentration and b) the actual data resulting from Butler-Volmer fitting current transients in varying buffer concentrations, repeated for three electrodes in each electrolyte.

Exchange current densities were then compared across the varied electrolyte buffer concentrations. If bisulfate acted as the proton donor, an increase in current corresponding to the magnitude of increasing buffer concentration would be expected. In the case that the reaction exhibited first-order kinetic dependence on the bisulfate proton donor, an increase in exchange current density with rising magnitude of bisulfate concentration would be anticipated, as illustrated in Figure 21a. Conversely, if the proton insertion reaction depended solely on the hydronium ions present, no variation in exchange current density would be expected, given that the pH was kept constant. The fact that all error bars in Figure 21b fall within a similar range and are of the same order of magnitude suggests that hydronium is the predominant proton donor in the potassium bisulfate buffer solution. Although changes in current were observed across

different concentrations in Figure 19, the buffered electrolyte concentration did not appear to influence the intrinsic reaction kinetics. This change in current in the CV response could be due to different adsorption character at the WO_3 but is not likely caused by enhanced proton insertion kinetics in higher concentrations of bisulfate.

Figure 22: Bisulfate Buffer and HCl Exchange Current Density Comparison

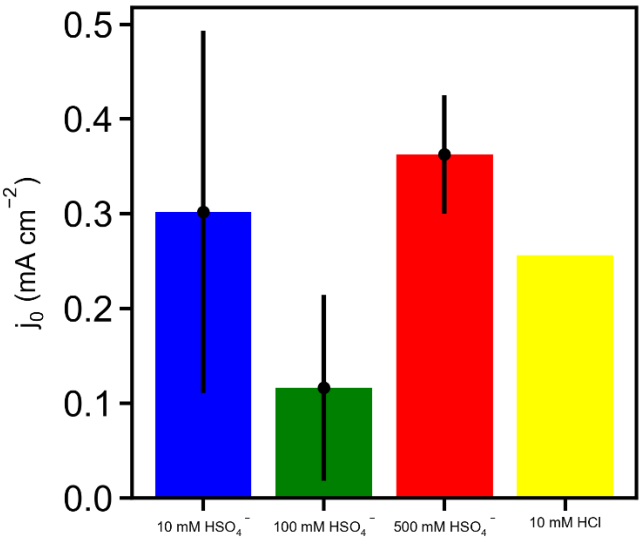

Figure 22: The data from Figure 21 with potassium bisulfate buffered electrolyte compared to one trial of proton insertion in 1 M HCl electrolyte, where the exchange current density is mostly within uncertainty of the other buffer concentrations, suggesting no dependence on the bisulfate proton donor. The HCl data has not been repeated, therefore no error bars were included for this data point.

The bisulfate donor was further eliminated as a possible proton donor when compared to the proton insertion kinetics in a pH 2 solution of HCl. The current transient experiment with Butler-Volmer fitting was repeated in a non-buffered environment with only one proton donor available from HCl. In Figure 22, the yellow bar represents the exchange current density of a proton insertion in a 10 mM HCl electrolyte at pH 2, with a 1 M ionic strength supplemented by potassium chloride supporting electrolyte. While there is no error bar for uncertainty, future repeated experiments would ideally supplement this result. The 10 mM HCl experiment

exhibited an exchange current density within the range of uncertainty for the exchange current densities of each bisulfate concentration. This further supports the conclusion that the bisulfate anion does not donate its proton in the proton insertion reaction of WO_3.

Comparison of Buffer Environments

Figure 27: Cyclic Voltammetry Comparisons Between Bisulfate and Phosphate Buffer Systems

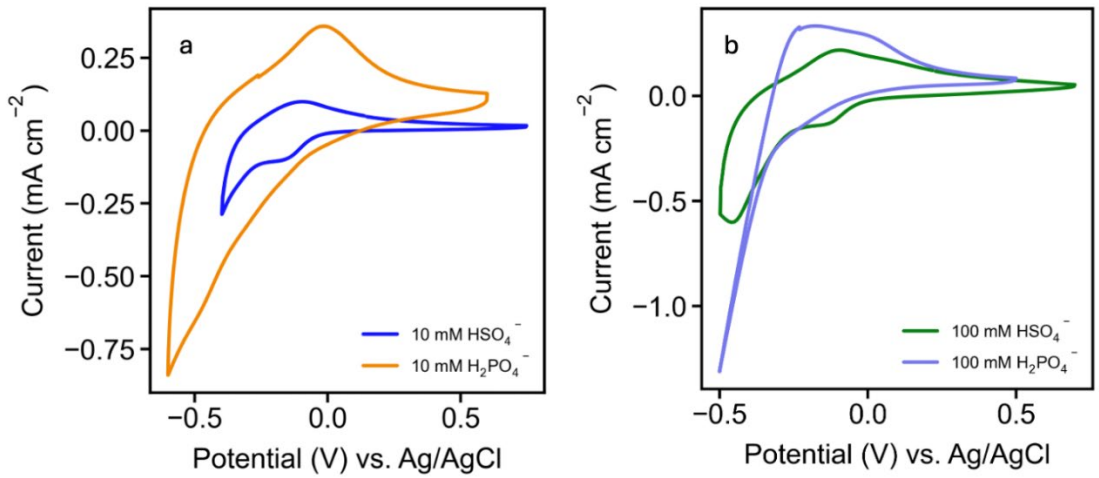

Figure 27: Cyclic voltammetry scans at 100 mV/s comparing the bisulfate buffer (pH, pKa = 1.99) and dihydrogen phosphate (pH, pKa = 2.15) for a) 10 mM concentration and b) 100 mM concentrations. Different electrodes were used, but all current is normalized to the area of the electrodes.

Both buffered proton donors were compared with their respective CVs and concentrations to identify any differences in activity due to the effect of electrolyte. Figure 27 shows the effect of electrolyte on cyclic voltammogram measurements in 10 mM and 100 mM buffer solutions. The dihydrogen phosphate buffer exhibits a higher capacitance, as seen in the spacing between anodic and cathodic regions. Additionally, the anodic peak is more prominent for the phosphoric acid buffer, while lacking the distinct cathodic A and A' peaks. Furthermore, HER current occurs at a lower onset than with the bisulfate buffer. In Figure 27b, the 100 mM phosphoric acid buffer displayed an unusual CV shape, also without the typical reduction

features of the double-staged proton insertion as observed in bisulfate. The larger magnitude of cathodic and anodic current suggests that tungsten oxide's reactivity is higher in the phosphoric acid buffer rather than the bisulfate buffer.

Figure 28: Comparison of Butler-Volmer Curves in Bisulfate and Phosphate Buffers

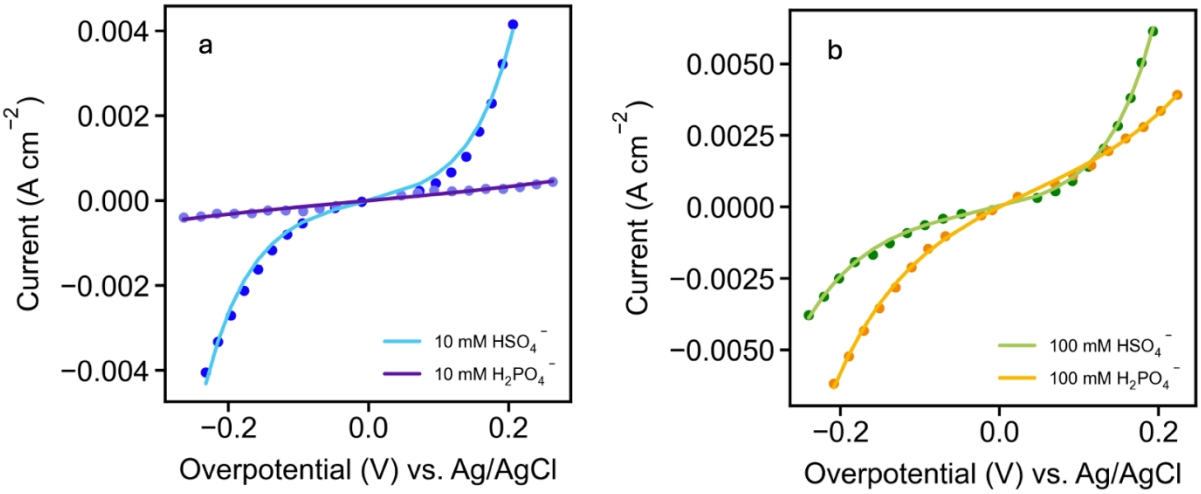

Figure 28: Comparison between the bisulfate and dihydrogen phosphate buffer solutions for a) 10 mM concentrations and b) 100 mM concentrations. The BV curves have been iR corrected for their series resistance relative to the electrode and the varying electrolyte solutions.

Furthermore, the Butler-Volmer curves were compared between each buffered proton donor solution in Figure 28. For the 10 mM buffer concentrations, the dihydrogen phosphate electrolyte shows a significantly lower current in response to overpotential than the bisulfate buffer. This result is inconsistent with the CVs in Figure 27, where there is more current for the phosphoric acid. This may be due to the phosphoric acid inducing more double-layer capacitance at the surface of the electrode, without increasing ion transfer current. This would cause the current transient fit to select a larger region of double layer charging. In Figure 28b, the 100 mM buffers show differences in anodic and cathodic current, where the dihydrogen phosphate buffer exhibits

a higher cathodic current, likely due to the earlier onset of HER as observed in the CVs of Figure 27b.

Figure 29: Comparing Exchange Current Densities Across Buffer Systems

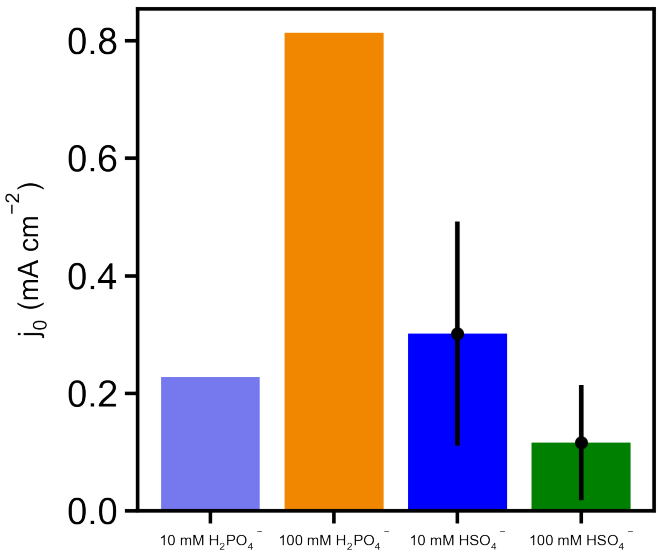

Figure 29: Bar graphs indicating the exchange current density for changing concentrations of dihydrogen phosphate buffer at pKa = 2.15 (orange and purple) and bisulfate at pKa = 1.99 (blue and green), stemming from the Butler-Volmer fitting current transients. There are no error bars for the dihydrogen phosphate buffers due to lack of repetition of the experiment.

The exchange current density from the phosphoric buffered proton donor electrolyte was compared to the bisulfate proton donor electrolyte. While the 10 mM dihydrogen phosphate buffer exhibits an exchange current density within error of both bisulfate buffered proton donors, the 100 mM dihydrogen phosphate buffer had a significant increase in exchange current density. It remains that this reaction does not follow a first order rate law, as discussed in Figure 21b, because there is not a ten-fold increase in exchange current density with a ten-fold increase in concentration. This implies that the dihydrogen phosphate ion is not the main proton donor in solution but could be competing with nearby hydroniums.

$$HSO_4^- + H_2O \rightarrow SO_4^{2-} + H_3O^+ \qquad \text{pKa} = 6.91$$

$$H_2PO_4^- + H_2O \rightarrow HPO_4^{2-} + H_3O^+ \qquad \text{pKa} = 7.21$$

The differences between the two buffers manifest in the identity of the central atom and the number of protons after the first proton removal. When sulfuric acid is buffered to its pKa with KOH, the first proton on H_2SO_4 is removed, leaving one proton on the proton donor, attached to an oxygen bonded to the central sulfur atom. Since phosphoric acid is triprotic, it will still have two protons after its first deprotonation, both attached to an oxygen atom bridging to the central phosphorus atom. Since the deprotonated phosphoric acid has two protons remaining, one might think it may be more energetically favorable for the phosphoric acid to donate its second proton. However, the pKa values of the second dissociation of each acid indicate that a second dissociation would be more favorable for sulfuric acid. This analysis indicates that pKa is not the driving force of proton donation within porous electrodes like tungsten oxide. While the exchange current densities do not follow the expected trend based on pKa, additional absorption effects on the electrode interface could explain the enhanced kinetics in the phosphoric acid buffer.

Looking into other trends like electronegativity or solvation shell, the observed kinetic trend is also contradicted. Electronegativity is the tendency of an atom to attract electrons, due to the atom's ability to stabilize the extra negative charges. The electronegativity trends upward and right within the periodic table, and within the third period in the periodic table, sulfur is situated to the right of phosphorus, indicating its higher electronegativity. The kinetic findings for the system of proton insertion into the tungsten oxide lattice showed that the bisulfate anion was not favorably deprotonated, while the dihydrogen phosphate anion was. This contradicts the trend of

electronegativity because one would expect the higher electronegativity to stabilize the negative charge induced by deprotonation better.

To explore the unexpected trends of this system, it is hypothesized that a supporting cation, like that of the supporting electrolyte and base titrate (potassium), could be not acting as an inert component of the system, but contributing to the support of the anion within the double layer. If this were the case, the potassium ion may be stabilizing the deprotonated dihydrogen phosphate anion, which in turn promotes the hydrogen insertion and/or evolution reactions in tungsten oxide. This may not be occurring in the bisulfate buffer, which is why such different current responses are observed in between the two buffer systems.

Conclusions and Broader Implications

This study advanced a new approach to studying how protons insert a WO_3 thin film, particularly concerning proton donor identity and concentration dependence. A robust kinetic analysis was developed, leading to the extrapolation of the ion transfer current through deconvolution of double-layer capacitance contributions. Butler-Volmer formalism was used to extract the kinetic information, such as exchange current densities, and charge transfer coefficients. This technique has the potential to be applied to an array of insertion materials, where their insertion kinetics can be further evaluated in different environments.

When different proton donor buffer solutions were used, it was found that in potassium bisulfate solutions, hydronium ions donate their protons, while in phosphoric acid, the concentration of proton donors has a small effect on reaction kinetics. These results suggest that different electrolytes can change how ion transfer happens at the surface of metal oxides. Understanding these differences is important for improving how materials like WO_3 are used in batteries and other charge storage technologies. Since phosphoric acid appears to promote both the proton insertion reaction and the hydrogen evolution reaction (HER) by lowering the applied overpotentials, these findings are relevant for water electrolysis. Electrolysis catalysts are often rare earth metals like platinum and iridium, but if earth-abundant WO_3 could be used as an alternative if HER overpotentials are lowered enough. More importantly, aqueous electrolytes have an effect on the insertion kinetics and electrocatalytic, which could be immensely useful for green electricity storage.

Future experiments should fine tune the data collection for the phosphoric acid buffer and separate the proton insertion current from the hydrogen evolution reaction. An expanded concentration window up to 500 mM, and possibly 1 M depending on the solubility limits of the buffer, should be used to measure the proton insertion kinetics with the previously developed method. Furthermore, the effect of supporting cation should be explored to understand the role of the phosphoric acid buffer at the surface. If a bulkier supporting cation is used, like tetramethylammonium (TMA), it may provide less support to the anion and reduce reaction rate of proton-electron exchange. Meanwhile, if a different alkali metal cation like lithium or sodium is used, the solvation shell could have a differing effect on the promotion of proton insertion for this electrode-electrolyte interface. Systematically changing the supporting cation here while maintaining the pH, as the buffer experiments have done, may provide insights into the role of the supposedly inert supporting cation.

Bibliography

(1) Roychowdhury, D.; D'Antona, N.; Zhao, Y.; Surendranath, Y.; Augustyn, V.; Kempler, P.; Boettcher, S. Interfacial Proton-Transfer Kinetics Using Model Tungsten Oxide Thin Films. ChemRxiv April 8, 2025. https://doi.org/10.26434/chemrxiv-2025-mh3bf.

(2) Summary for Policymakers. In *Climate Change 2021 – The Physical Science Basis: Working Group I Contribution to the Sixth Assessment Report of the Intergovernmental Panel on Climate Change*; Intergovernmental Panel on Climate Change (IPCC), Ed.; Cambridge University Press: Cambridge, 2023; pp 3–32. https://doi.org/10.1017/9781009157896.001.

(3) US EPA, O. *Inventory of U.S. Greenhouse Gas Emissions and Sinks*. https://www.epa.gov/ghgemissions/inventory-us-greenhouse-gas-emissions-and-sinks (accessed 2025-05-06).

(4) *The Paris Agreement | UNFCCC*. https://unfccc.int/process-and-meetings/the-paris-agreement (accessed 2024-05-06).

(5) Rockström, J.; Gaffney, O.; Rogelj, J.; Meinshausen, M.; Nakicenovic, N.; Schellnhuber, H. J. A Roadmap for Rapid Decarbonization. *Science* **2017**, *355* (6331), 1269–1271.

(6) Global Energy Review 2025. **2025**.

(7) Cabana, J.; Alaan, T.; Crabtree, G. W.; Huang, P.-W.; Jain, A.; Murphy, M.; N'Diaye, J.; Ojha, K.; Agbeworvi, G.; Bergstrom, H.; Gersib, S.; Harb, H.; Stejer, A.; Quiles-Galarza, G.; Rodriguez, O.; Caruso, I.; Gonçalves, J. M.; Chen, G. Y.; Fernández, C. A.; Pan, H.; Ritter, K.; Yang, Y.; Zhang, H.; García-Álvarez, A. C.; Ilic, S.; Kumar, K.; Silcox, R.; Yao, Y.; Song, H.; Stoyanov, S.; Saraf, M.; Chen, C. H.; Subasinghe, S. M. S.; Gomes, R.; Lang, S.; Murphy, E.; Thind, A. S.; Zheng, Y. NGenE 2022: Electrochemistry for Decarbonization. *ACS Energy Lett.* **2023**, *8* (1), 740–747. https://doi.org/10.1021/acsenergylett.2c02587.

(8) Xia, R.; Overa, S.; Jiao, F. Emerging Electrochemical Processes to Decarbonize the Chemical Industry. *JACS Au* **2022**, *2* (5), 1054–1070. https://doi.org/10.1021/jacsau.2c00138.

(9) *WO3 quantum-dots electrochromism - 10815064.pdf*. https://www.reprintsdesk.com/userv3/fulltextreader.aspx (accessed 2024-05-06).

(10) Nguyen, V.-T.; Min, B. K.; Kim, S. K.; Yi, Y.; Choi, C.-G. A Flexible and High-Performance Electrochromic Smart Window Produced by WO3/Ti3C2Tx MXene Hybrids. *J. Mater. Chem. C* **2021**, *9* (9), 3183–3192. https://doi.org/10.1039/D0TC05547F.

(11) Thomas, S. A.; Cherusseri, J.; Khalid, M. A Comprehensive Review on Tungsten Oxide Nanostructures-Based Electrochromic Supercapacitors and Machine Learning Models for Design and Process Parameter Optimization. *Energy Storage* **2023**, *5* (8), e499. https://doi.org/10.1002/est2.499.

(12) *Tungsten Oxides for Photocatalysis, Electrochemistry, and Phototherapy - Huang - 2015 - Advanced Materials - Wiley Online Library*. https://onlinelibrary.wiley.com/doi/10.1002/adma.201501217 (accessed 2023-11-14).

(13) Shinde, P. A.; Jun, S. C. Review on Recent Progress in the Development of Tungsten Oxide Based Electrodes for Electrochemical Energy Storage. *ChemSusChem* **2020**, *13* (1), 11–38. https://doi.org/10.1002/cssc.201902071.

(14) Hölzle, M. H.; Zwing, V.; Kolb, D. M. The Influence of Steps on the Deposition of Cu onto Au(111). *Electrochimica Acta* **1995**, *40* (10), 1237–1247. https://doi.org/10.1016/0013-4686(95)00055-J.

(15) Miu, E. V.; McKone, J. R.; Mpourmpakis, G. The Sensitivity of Metal Oxide Electrocatalysis to Bulk Hydrogen Intercalation: Hydrogen Evolution on Tungsten Oxide. *J. Am. Chem. Soc.* **2022**, *144* (14), 6420–6433. https://doi.org/10.1021/jacs.2c00825.
(16) Nikitina, V. A.; Vassiliev, S. Y.; Stevenson, K. J. Metal-Ion Coupled Electron Transfer Kinetics in Intercalation-Based Transition Metal Oxides. *Adv. Energy Mater.* **2020**, *10* (22), 1903933. https://doi.org/10.1002/aenm.201903933.
(17) Mitchell, J. B.; Lo, W. C.; Genc, A.; LeBeau, J.; Augustyn, V. Transition from Battery to Pseudocapacitor Behavior via Structural Water in Tungsten Oxide. *Chem. Mater.* **2017**, *29* (9), 3928–3937. https://doi.org/10.1021/acs.chemmater.6b05485.
(18) Lin, H.; Zhou, F.; Liu, C.-P.; Ozoliņš, V. Non-Grotthuss Proton Diffusion Mechanism in Tungsten Oxide Dihydrate from First-Principles Calculations. *J. Mater. Chem. A* **2014**, *2* (31), 12280–12288. https://doi.org/10.1039/C4TA02465F.
(19) Huynh, M. H. V.; Meyer, T. J. Proton-Coupled Electron Transfer. *Chem. Rev.* **2007**, *107* (11), 5004–5064. https://doi.org/10.1021/cr0500030.
(20) Bard, A. J.; Faulkner, L. R.; White, H. S.; Bard, A. J. *Electrochemical Methods: Fundamentals and Applications*, Third edition.; Wiley: Hoboken, NJ, 2022.
(21) Henstridge, M. C.; Laborda, E.; Rees, N. V.; Compton, R. G. Marcus–Hush–Chidsey Theory of Electron Transfer Applied to Voltammetry: A Review. *Electrochimica Acta* **2012**, *84*, 12–20. https://doi.org/10.1016/j.electacta.2011.10.026.
(22) Bai, P.; Bazant, M. Z. Charge Transfer Kinetics at the Solid–Solid Interface in Porous Electrodes. *Nat. Commun.* **2014**, *5* (1), 3585. https://doi.org/10.1038/ncomms4585.
(23) Chekushkin, P. M.; Merenkov, I. S.; Smirnov, V. S.; Kislenko, S. A.; Nikitina, V. A. The Physical Origin of the Activation Barrier in Li-Ion Intercalation Processes: The Overestimated Role of Desolvation. *Electrochimica Acta* **2021**, *372*, 137843. https://doi.org/10.1016/j.electacta.2021.137843.
(24) Lewis, N. B.; Bisbey, R. P.; Westendorff, K. S.; Soudackov, A. V.; Surendranath, Y. A Molecular-Level Mechanistic Framework for Interfacial Proton-Coupled Electron Transfer Kinetics. *Nat. Chem.* **2024**, *16* (3), 343–352. https://doi.org/10.1038/s41557-023-01400-0.
(25) Jackson, M. N.; Jung, O.; Lamotte, H. C.; Surendranath, Y. Donor-Dependent Promotion of Interfacial Proton-Coupled Electron Transfer in Aqueous Electrocatalysis. *ACS Catal.* **2019**, *9* (4), 3737–3743. https://doi.org/10.1021/acscatal.9b00056.
(26) Lazanas, A. Ch.; Prodromidis, M. I. Electrochemical Impedance Spectroscopy─A Tutorial. *ACS Meas. Sci. Au* **2023**, *3* (3), 162–193. https://doi.org/10.1021/acsmeasuresciau.2c00070.